

Neutrino Emissions from Tidal Disruption Remnants

Kimitake HAYASAKI¹ and Ryo YAMAZAKI²

kimi@cbnu.ac.kr

Received _____; accepted _____

¹Department of Astronomy and Space Science, Chungbuk National University, Cheongju 361-763, Korea

²Department of Physics and Mathematics, Aoyama Gakuin University, 5-10-1, Fuchinobe, Sagamihara 252-5258, Japan

ABSTRACT

We study high-energy neutrino emissions from tidal disruption remnants (TDRs) around supermassive black holes. The neutrinos are produced by the decay of charged pions originating in ultrarelativistic protons that are accelerated there. In the standard theory of tidal disruption events (TDEs), there are four distinct phases from debris circularization of stellar debris to super- and sub-Eddington to radiatively inefficient accretion flows (RIAFs). In addition, we consider the magnetically arrested disk (MAD) state in both the super-Eddington accretion and RIAF phases. We find that there are three promising cases to produce neutrino emissions: the super-Eddington accretion phase of the MAD state and the RIAF phases of both the non-MAD and MAD states. In the super-Eddington MAD state, the enhanced magnetic field makes it possible to accelerate the protons to $E_{p,\max} \sim 0.35 \text{ PeV} (M_{\text{bh}}/10^{7.7} M_{\odot})^{41/48}$ with the other given appropriate parameters. The neutrino energy is then $E_{\nu,\text{pk}} \sim 67 \text{ TeV} (M_{\text{bh}}/10^{7.7} M_{\odot})^{41/48}$ at the peak of the energy spectrum. For $M_{\text{bh}} \gtrsim 10^{7.7} M_{\odot}$, the neutrino light curve is proportional to $t^{-65/24}$, while it follows the standard $t^{-5/3}$ decay rate for $M_{\text{bh}} < 10^{7.7} M_{\odot}$. In both cases, the large luminosity and characteristic light curves diagnose the super-Eddington MAD state in TDEs. In the RIAF phase of the non-MAD state, we find $E_{p,\max} \sim 0.45 \text{ PeV} (M_{\text{bh}}/10^7 M_{\odot})^{5/3}$ and $E_{\nu,\text{pk}} \sim 0.35 \text{ PeV} (M_{\text{bh}}/10^7 M_{\odot})^{5/3}$, and its light curve is proportional to $t^{-10/3}$. This indicates that one can identify whether the existing RIAFs are the TDE origin or not. TDRs are potentially a population of hidden neutrino sources invisible in gamma rays.

Subject headings: acceleration of particles – neutrinos – accretion, accretion disks – black hole physics – galaxies: nuclei

1. Introduction

A recent discovery of very high energy (VHE) neutrinos in the TeV-PeV energy range by IceCube (Aartsen et al. 2013) has motivated the neutrino astronomy and astrophysics. Because the astrophysical neutrinos originate from cosmic-ray hadronic interactions, the detection of the neutrinos simultaneously gives us the information about the sources of the high-energy cosmic-ray nuclei. There are several astrophysical candidates for their origination: active galactic nuclei (AGNs), galaxy clusters/groups, starburst galaxies, supernovae and hypernovae, gamma-ray bursts (GRBs), white dwarf (WD) mergers, and tidal disruption events (TDEs; for a review see Mészáros 2017).

TDEs are thought to be a key phenomenon in the search for dormant supermassive black holes (SMBHs) at the centers of the inactive galaxies and for unidentified intermediate-mass black holes (IMBHs) at the centers of star clusters. Most TDEs take place when a star at a large separation is perturbed onto a parabolic orbit approaching close enough to the SMBH to be ripped apart by its tidal force. The subsequent accretion of stellar debris falling back to the SMBH causes a characteristic flare with a luminosity large enough to exceed the Eddington luminosity for a time scale of weeks to months (Rees 1988; Evans & Kochanek 1989; Phinney 1989; Lodato et al. 2009). Such flares have been discovered at optical (Gezari et al. 2012; Arcavi et al. 2014; Holoien et al. 2014, 2016; Hung et al. 2017), ultraviolet (Gezari et al. 2006; Chornock et al. 2014; Vinkó et al. 2015), and soft X-ray (Komossa & Bade 1999; Saxton et al. 2012; Maksym et al. 2013; Auchetl et al. 2017) wavebands with inferred event rates of $10^{-5} - 10^{-4}$ per year per galaxy (Donley et al. 2002; Wang & Merritt 2004; van Velzen & Farrar 2014; Stone & Metzger 2016). The other high-energy jetted TDEs have been detected through nonthermal emissions in radio (Zauderer et al. 2011; Alexander et al. 2016; van Velzen et al. 2016) or hard X-ray (Burrows et al. 2011; Brown et al. 2015) wavebands with much lower

event rates (Farrar & Piran 2014). The best observed jetted TDE is Swift J1644+57 (Burrows et al. 2011); others are Swift J2058.4+0516 (Cenko et al. 2012) and Swift J1112.2-8238 (Brown et al. 2015). The observed diversity of these optical to X-ray TDEs can be explained in part by the viewing angle of the observer relative to the orientation of the disk angular momentum (Dai et al. 2018).

The origin of ultrahigh-energy cosmic rays (UHECRs) is still open to discussion. Possible candidates of UHECR accelerators are GRBs (Waxman 1995), the short-duration bursts of AGNs (Farrar & Gruzinov 2009), and so forth. The jetted TDEs can also be candidate sources of UHECRs (Farrar & Piran 2014; Pfeffer et al. 2017). Recent observations with the Pierre Auger Observatory suggest that the compositions of UHECRs can be metal rich (Aab et al. 2017). The tidal disruption of a WD by an IMBH is proposed as a UHECR source to satisfy the heavy nuclei requirement (Alves Batista & Silk 2017; Zhang et al. 2017).

The neutrinos are naturally produced from the UHECRs by pionic decay. Such high-energy neutrino flux was predicted by Murase (2008) following the scenario of Farrar & Gruzinov (2009) and for targeting Swift J1644+57 by Wang et al. (2011). After the detection of the IceCube neutrinos, the contribution of the jetted TDEs on the observed neutrino flux was examined (Senno et al. 2017; Lunardini & Winter 2017; Dai & Fang 2017). Jetted TDEs can be a population of cosmic-ray accelerators, which are not visible in GeV-TeV gamma-rays, that serve as the origin of TeV-PeV neutrinos (Murase et al. 2016; Wang & Liu 2016; Murase & Fukugita 2019). Whether they are a common source of both UHECRs and neutrinos has also been debated (Guépin et al. 2018; Biehl et al. 2018). However, little is known about such high-energy emissions from the nonjetted parts including the disk components in TDEs, although some sites seem to be good candidates for the production of high-energy particles because of the shock formation and the high-energy

density around the forming disk during the event.

In this work, we examine the stochastic acceleration of the protons by magnetic turbulence and subsequent high-energy neutrino emissions from a tidally disrupted star (or a tidal disruption remnant (TDR)). In Section 2, we discuss the possible sites at which the ultrarelativistic protons can be produced during a TDE. In Section 3, we calculate the energy spectral distributions and luminosities of the protons, gamma-rays, and neutrinos produced by pionic decay, although the gamma-rays cannot be emitted because of the highly opaque remnant. We discuss our results in Section 4. Section 5 is devoted to the conclusion of our scenario.

2. High-energy emission sites after tidal disruption of a star

After the tidal disruption of a star, the stellar debris falls back onto an SMBH and is circularized by the shock dissipation to convert the orbital energy into thermal energy by a collision between the debris head and tail. This naturally leads to the formation of an accretion disk around the black hole (Hayasaki et al. 2013; Bonnerot et al. 2016; Hayasaki et al. 2016), although the detailed dissipation mechanism is still being debated (Shiokawa et al. 2015; Piran et al. 2015). If the accretion rate follows the standard $t^{-5/3}$ decay rate, a TDE can be divided by the accretion timescale into the four main evolutionary phases (see equation 16). In this section, we will discuss the possibility that protons can accelerate to the ultrarelativistic energies in each phase.

The tidal disruption radius, r_t , is given by

$$\frac{r_t}{r_S} = \left(\frac{M_{\text{bh}}}{m_*} \right)^{1/3} \frac{r_*}{r_S} \approx 5.1 \left(\frac{M_{\text{bh}}}{10^7 M_\odot} \right)^{-2/3} \left(\frac{m_*}{M_\odot} \right)^{-1/3} \left(\frac{r_*}{R_\odot} \right), \quad (1)$$

where M_{bh} is mass of the central SMBH, m_* and r_* are the stellar mass and radius, and $r_S = 2GM_{\text{bh}}/c^2$ is the Schwarzschild radius of the SMBH, and c is the speed of light.

This angular momentum conservation allows us to estimate the circularization radius of the stellar debris, which is given by

$$r_{\text{circ}} = a_*(1 - e_*^2) = (1 + e_*)r_{\text{p}}, \quad (2)$$

where a_* and e_* are the semi-major axis and the orbital eccentricity of the star, respectively. The pericenter distance, $r_{\text{p}} = a_*(1 - e_*)$, is also written by

$$r_{\text{p}} = \frac{r_{\text{t}}}{\beta}, \quad (3)$$

where β is the penetration factor, that is, the ratio of tidal disruption to pericenter radii. The specific binding energy of the stellar debris measured at r_{circ} can be then given by

$$\epsilon_{\text{circ}} = -\frac{1}{2} \frac{1}{1 + e_*} \frac{GM_{\text{bh}}}{r_{\text{p}}}. \quad (4)$$

On the other hand, the specific orbital energy of the star is

$$\epsilon_* = -\frac{(1 - e_*)}{2} \frac{GM_{\text{bh}}}{r_{\text{p}}}. \quad (5)$$

The difference between $m_*\epsilon_*$ and $m_*\epsilon_{\text{circ}}$ gives the maximum amount of binding energy potentially dissipated during debris circularization:

$$\begin{aligned} \Delta\epsilon_{\text{circ}} &= m_*|\epsilon_* - \epsilon_{\text{circ}}| = \frac{m_*}{2} \frac{e_*^2}{(1 + e_*)} \frac{GM_{\text{bh}}}{r_{\text{p}}} \sim 4.4 \times 10^{52} \text{ erg} \\ &\times \left(\frac{\beta}{1.0}\right) \left(\frac{m_*}{M_{\odot}}\right)^{4/3} \left(\frac{r_*}{R_{\odot}}\right)^{-1} \left(\frac{M_{\text{bh}}}{10^7 M_{\odot}}\right)^{2/3} \end{aligned} \quad (6)$$

for $e_* \approx 1.0$ stellar orbits.

Let us assume that the dissipated energy during the debris circularization is proportional to the mass fallback rate:

$$L_{\text{circ}} = \eta_{\text{circ}} \dot{M}_{\text{fb}} c^2, \quad (7)$$

where η_{circ} is the mass-to-energy conversion efficiency of the debris circularization and

$$\dot{M}_{\text{fb}} = \frac{1}{3} \frac{m_*}{t_{\text{mtb}}} \left(\frac{t}{t_{\text{mtb}}}\right)^{-5/3} \sim 5.9 \times 10^{25} \text{ g s}^{-1} \left(\frac{M_{\text{bh}}}{10^7 M_{\odot}}\right)^{-1/2} \left(\frac{m_*}{M_{\odot}}\right)^2 \left(\frac{r_*}{R_{\odot}}\right)^{-3/2} \quad (8)$$

is the mass fallback rate (Evans & Kochanek 1989). Here t_{mtb} is the orbital period of the stellar debris on the most tightly bound orbit:

$$t_{\text{mtb}} = \frac{\pi}{\sqrt{2}} \frac{1}{\Omega_*} \left(\frac{M_{\text{bh}}}{m_*} \right)^{1/2} \approx 1.1 \times 10^7 \text{ s} \left(\frac{M_{\text{bh}}}{10^7 M_\odot} \right)^{1/2} \left(\frac{m_*}{M_\odot} \right)^{-1} \left(\frac{r_*}{R_\odot} \right)^{3/2}, \quad (9)$$

where $\Omega_* = \sqrt{Gm_*/r_*^3}$ is the dynamical angular frequency of the star. By using equations (6)-(8), we define the circularization timescale as

$$\begin{aligned} t_{\text{circ}} \equiv \frac{\Delta \epsilon_{\text{circ}}}{L_{\text{circ}}(t_{\text{circ}})} &= \left(\frac{4}{3} \frac{\eta_{\text{circ}}}{\beta} \frac{(1+e_*)}{e_*^2} \frac{r_t}{r_s} \right)^{3/2} t_{\text{mtb}} \\ &\sim 1.8 \times 10^7 \text{ s} \left(\frac{\eta_{\text{circ}}}{0.1} \right)^{3/2} \left(\frac{\beta}{1.0} \right)^{-3/2} \left(\frac{M_{\text{bh}}}{10^7 M_\odot} \right)^{-1/2} \left(\frac{r_*}{R_\odot} \right)^3 \left(\frac{m_*}{M_\odot} \right)^{-3/2} \end{aligned} \quad (10)$$

for $e_* \approx 1$. Because t_{circ} should be longer than t_{mtb} so that the debris circularization starts after the most tightly bound debris firstly falls back to the black hole, η_{circ} should be larger than a certain critical value η_0 , which is given by

$$\eta_0 = \frac{3\beta}{4} \frac{e_*^2}{1+e_*} \frac{r_s}{r_t} \sim 7.4 \times 10^{-2} \left(\frac{\beta}{1.0} \right) \left(\frac{M_{\text{bh}}}{10^7 M_\odot} \right)^{2/3} \left(\frac{r_*}{R_\odot} \right)^{-1} \left(\frac{m_*}{M_\odot} \right)^{1/3} \quad (11)$$

for $e_* \approx 1$. If the debris circularization is done only through the shock dissipation by the debris self-crossings, the circularization timescale for nonmagnetized stellar debris can be estimated as $t_{\text{circ}} \approx 8.3 (M_{\text{bh}}/10^6 M_\odot)^{-3/5} \beta^{-3} t_{\text{mtb}}$ based on the ballistic approximation (Bonnerot et al. 2017). Equating this equation with equation (10), we can evaluate the circularization efficiency as

$$\eta_{\text{circ}} \sim 1.6 \left(\frac{1.0}{\beta} \right)^{-2} \left(\frac{M_{\text{bh}}}{10^7 M_\odot} \right)^{-2/5} \eta_0. \quad (12)$$

This is applicable if the black hole mass is less than $\sim 3.4 \times 10^7 (\beta/1.0)^{-5} M_\odot$ because of $\eta_{\text{circ}} > \eta_0$.

Now we define the normalized accretion rate by

$$\dot{m} \equiv \frac{\dot{M}}{\dot{M}_{\text{Edd}}}, \quad (13)$$

where $\dot{M}_{\text{Edd}} = L_{\text{Edd}}/c^2 \sim 1.4 \times 10^{24} \text{ g s}^{-1} (M_{\text{bh}}/10^7 M_{\odot})$ and $L_{\text{Edd}} = 4\pi G M_{\text{bh}} m_p c / \sigma_{\text{T}}$ is the Eddington luminosity, m_p is the proton mass, and σ_{T} is the Thomson scattering cross section. We can estimate the time when it takes from super-Eddington to sub-Eddington accretion as

$$t_{\text{Edd}} = \left(\frac{1}{3} \frac{m_*}{t_{\text{mtb}}} \frac{1}{\dot{M}_{\text{Edd}}} \right)^{3/5} t_{\text{mtb}} \sim 1.1 \times 10^8 \text{ s} \left(\frac{M_{\text{bh}}}{10^7 M_{\odot}} \right)^{-2/5} \left(\frac{m_*}{M_{\odot}} \right)^{1/5} \left(\frac{r_*}{R_{\odot}} \right)^{3/5} \quad (14)$$

by substituting equation (8) into equation (13) with $\dot{m} = 1$. Because $t_{\text{circ}}/t_{\text{Edd}} \sim 0.17 (\eta_{\text{circ}}/0.1)^{3/2} (\beta/1.0)^{-3/2} (M_{\text{bh}}/10^7 M_{\odot})^{-1/10} (m_*/M_{\odot})^{-17/10} (r_*/R_{\odot})^{12/5}$ is smaller than 1, the circularization phase is shorter than the super-Eddington accretion phase. As time goes by, \dot{m} decreases to 0.01, and at this point the accretion disk enters the radiatively inefficient accretion flow (RIAF) phase. We set a time of onset of the RIAF phase at $\dot{m} = 0.01$ as

$$t_{\text{RIAF}} = \dot{m}^{-3/5} t_{\text{Edd}} \sim 1.7 \times 10^9 \text{ s} \left(\frac{\dot{m}}{0.01} \right)^{-3/5} \left(\frac{M_{\text{bh}}}{10^7 M_{\odot}} \right)^{-2/5} \left(\frac{m_*}{M_{\odot}} \right)^{1/5} \left(\frac{r_*}{R_{\odot}} \right)^{3/5}. \quad (15)$$

Here we divide the TDR into the four evolutionary phases:

$$\left\{ \begin{array}{ll} t_{\text{mtb}} < t \lesssim t_{\text{circ}} & \text{Circularization phase} \\ t_{\text{circ}} \lesssim t \lesssim t_{\text{Edd}} & \text{Super-Eddington accretion phase} \\ t_{\text{Edd}} \lesssim t \lesssim t_{\text{RIAF}} & \text{Sub-Eddington accretion phase} \\ t_{\text{RIAF}} \lesssim t & \text{RIAF phase.} \end{array} \right. \quad (16)$$

If a star on a marginally hyperbolic orbit is tidally disrupted by an SMBH, the RIAF phase would start right after the circularization phase without going through both the super-Eddington and sub-Eddington accretion phases (Hayasaki et al. 2018).

For the standard disk model, the number density is given by

$$n_p = \frac{\dot{M}}{2\pi m_p v_r r^2}, \quad (17)$$

where the radial drift velocity is given by

$$v_r \approx \alpha v_K \left(\frac{H}{r} \right)^2 \quad (18)$$

with the Shakura-Sunyaev viscosity parameter α , Keplerian velocity $v_K(r) = \sqrt{GM/r}$, and the disk thickness H . Note that the geometrically thin disk approximation that $H/r \sim 0.01$ is adopted for the standard disk. The accretion time is then given by

$$t_{\text{inf}} = \frac{r}{v_r} = \frac{r}{\alpha v_K} \left(\frac{H}{r} \right)^{-2} \sim 1.6 \times 10^8 \text{ s} \left(\frac{\alpha}{0.1} \right) \left(\frac{H/r}{0.01} \right)^{-2} \left(\frac{M_{\text{bh}}}{10^7 M_\odot} \right)^{-1/2} \left(\frac{r}{r_p} \right)^{3/2}. \quad (19)$$

The proton-proton relaxation timescale is estimated as

$$\begin{aligned} t_{\text{rel}} &= \frac{4\sqrt{\pi}}{\tau_p \ln \Lambda} \left(\frac{m_p}{m_e} \right)^2 \left(\frac{k_B T}{m_p c^2} \right)^{3/2} \frac{r}{c} \\ &\sim 5.7 \times 10^6 \text{ s} \left(\frac{\alpha}{0.1} \right) \left(\frac{20}{\ln \Lambda} \right) \left(\frac{\dot{m}}{0.1} \right)^{-1} \left(\frac{M_{\text{bh}}}{10^7 M_\odot} \right) \left(\frac{r}{r_p} \right)^{-3/2}, \end{aligned} \quad (20)$$

where $\tau_p = n_p \sigma_T r$, $\ln \Lambda$, and m_e are the optical depth for Thomson scattering, the Coulomb logarithm, and the electron mass, respectively. Here we assume the kinetic energy is completely converted to the thermal energy. The resultant proton's temperature is given by $k_B T = (1/3)GM_{\text{bh}}/r$.

The Coulomb loss time is given by equation (29) of Dermer et al. (1996) as

$$t_{\text{Coul}} = \frac{1225}{\tau_p \ln \Lambda} \frac{(\gamma - 1)}{(v_p/c)^2} \left[3.8\theta_e^{3/2} + \left(\frac{v_p}{c} \right)^3 \right] \frac{r}{c}, \quad (21)$$

where $\gamma = 1/\sqrt{1 - (v_p/c)^2}$ is the Lorentz factor of the proton with velocity v_p , and $\theta_e = k_B T_e/(m_e c^2)$ is the normalized electron temperature. Adopting $\gamma \sim 10$, $v_p/c \approx 1$, and $\theta_e \ll v_p/c$ in equation (21), we obtain

$$\begin{aligned} t_{\text{Coul}} &\approx \frac{1225}{\tau_p \ln \Lambda} \frac{(\gamma - 1)\sqrt{\gamma^2 - 1}}{\gamma} \frac{r}{c} \\ &\sim 4.4 \times 10^5 \text{ s} \left(\frac{\alpha}{0.1} \right) \left(\frac{20}{\ln \Lambda} \right) \left(\frac{\dot{m}}{0.1} \right)^{-1} \left(\frac{M_{\text{bh}}}{10^7 M_\odot} \right)^{-1/2} \left(\frac{r}{r_p} \right)^{3/2}. \end{aligned} \quad (22)$$

Since both t_{rel} and t_{Coul} are clearly shorter than the accretion timescale for the typical parameters during the sub-Eddington accretion phase, the plasma is collisional, so that nonthermal, high-energy protons are unlikely to be accelerated¹. Therefore, we will consider the other possible sites of the TDR that produce high-energy emissions in the following sections.

2.1. Collision of stellar debris after the tidal disruption

When the stellar debris passes through the pericenter distance, it significantly changes the trajectory of the debris by general relativistic apsidal precession (Rees 1988; Hayasaki et al. 2013). According to Jiang et al. (2016), the most tightly bound debris experiences the relativistic perihelion shift by the angle per orbit,

$$\omega_S = \frac{3\pi}{(1 + e_{\text{mtb}})} \frac{r_S}{r_p} \approx \frac{3\pi}{2} \frac{r_S}{r_p} \quad (23)$$

to the lowest post-Newtonian order (Merritt et al. 2010), where $e_{\text{mtb}} \approx 1$ is the debris eccentricity of the most tightly bound orbit. The radial distance of the stream-stream collision from the SMBH, where the debris collides with each other for the first time after the tidal disruption, can be written with equation (23) by (see Dai et al. 2015)

$$r_c = \frac{a(1 - e_{\text{mtb}}^2)}{(1 - e_{\text{mtb}} \cos(\omega_S/2))} \approx \frac{16}{\omega_S^2} r_p = \frac{64}{9\pi^2} \left(\frac{r_p}{r_S}\right)^2 r_p, \quad (24)$$

where we assume that $e_{\text{mtb}} \approx 1$ and $\omega_S \ll \pi$.

Since the stellar debris moves on a highly eccentric orbit, the debris velocity at r_c is estimated to be

$$v_c = v_K(r_c) \approx \frac{3\pi}{8\sqrt{2}} \left(\frac{r_p}{r_S}\right)^{-3/2} c. \quad (25)$$

¹See also panel (c) of Figure 1, where the characteristic timescales including these three are compared with the acceleration's timescale.

Assuming that the debris stream expands homologously, the radius of the stream cross section is given by

$$R(r_c) = \left(\frac{r_c}{r_p}\right) r_* \approx \frac{64}{9\pi^2} \left(\frac{r_p}{r_s}\right)^2 r_* \sim 1.3 \times 10^{12} \text{ cm} \left(\frac{r_*}{R_\odot}\right) \left(\frac{r_p}{r_s}\right)^2. \quad (26)$$

The proton's number density at r_c is given by

$$n_p = \frac{\dot{M}}{m_p v_c \sigma_c} \sim 1.6 \times 10^{15} \text{ cm}^{-3} \left(\frac{\dot{m}}{\dot{m}_{\text{fb}}}\right) \left(\frac{M_{\text{bh}}}{10^6 M_\odot}\right)^{-1/2} \left(\frac{r_p}{r_s}\right)^{-5/2}, \quad (27)$$

where $\sigma_c = \pi R(r_c)^2$ is the cross section of the return debris and we obtain \dot{m}_{fb}

$$\dot{m}_{\text{fb}} = \frac{\dot{M}_{\text{fb}}(t_{\text{mtb}})}{\dot{M}_{\text{Edd}}} \sim 42 \left(\frac{M_{\text{bh}}}{10^7 M_\odot}\right)^{-3/2} \left(\frac{m_*}{M_\odot}\right)^2 \left(\frac{r_*}{R_\odot}\right)^{-3/2} \quad (28)$$

by using equations (8), (9), and (13).

Now we examine whether the first-order particle (Fermi) acceleration is efficient at the shock. The mean free path of the photons, during which they can travel until colliding with the protons, is estimated to be

$$l_\nu = \frac{1}{n_p \sigma_T} \sim 9.6 \times 10^8 \text{ cm} \left(\frac{\dot{m}}{\dot{m}_{\text{fb}}}\right)^{-1} \left(\frac{M_{\text{bh}}}{10^7 M_\odot}\right)^{1/2} \left(\frac{r_p}{r_s}\right)^{5/2}. \quad (29)$$

The Larmor radius of the proton of $\gamma(v_p/c) \sim 1$ is given by

$$r_L \sim \frac{m_p c^2}{q_e B}, \quad (30)$$

where q_e is the electric charge and B is the magnetic field strength. It is obtained with the plasma beta \mathcal{B} based on the energy equipartition assumption by

$$B = \sqrt{\frac{8\pi m_p n_p k_B T}{\mathcal{B}}} = \left(\frac{8\pi}{3\mathcal{B}}\right)^{1/2} \sqrt{\rho_p v_K(r)^2}, \quad (31)$$

where $\rho_p = m_p n_p$ is the proton's mass density. The ratio of the mean free path to the Larmor radius at r_c is estimated to be

$$\begin{aligned} \frac{l_\nu}{r_L} &= \frac{q_e B}{n_p m_p c^2 \sigma_T} = \frac{q_e}{n_p m_p c^2 \sigma_T} \left(\frac{8\pi}{3\mathcal{B}}\right)^{1/2} \sqrt{\frac{GM m_p n_p}{r_c}} \sim 5.7 \times 10^7 \left(\frac{\mathcal{B}}{3}\right)^{-1/2} \\ &\times \left(\frac{\dot{m}}{\dot{m}_{\text{fb}}}\right)^{-1/2} \left(\frac{M_{\text{bh}}}{10^7 M_\odot}\right)^{1/4} \left(\frac{m_*}{M_\odot}\right)^{-1} \left(\frac{r_*}{R_\odot}\right)^{7/4} \left(\frac{r_p}{r_s}\right)^{-3/4} \left(\frac{r_c}{r_p}\right)^{1/4}. \end{aligned} \quad (32)$$

It is noted from equations (26), (29), and (32) that $r_L \ll l_\nu \ll R(r_c)$. The radiation-mediated shock should be formed at the first shock of debris circularization, leading to the inefficient first-order Fermi acceleration there (Waxman & Loeb 2001; Murase & Ioka 2013).

Next we discuss the possibility of causing the second-order Fermi acceleration in the magnetic turbulence that is excited during the debris circularization phase. The characteristic timescales for the second-order Fermi acceleration of the protons are evaluated by (Kimura et al. 2015)

$$t_{\text{acc1}} = \frac{1}{\zeta} \frac{r}{c} \left(\frac{v_A}{c} \right)^{-2} \left(\frac{r_L}{r} \right)^{2-s} \gamma^{2-s}, \quad (33)$$

where ζ shows the ratio of the strength of turbulent fields to that of the nonturbulent fields, s is a spectral index of the turbulence, and the Alfvén speed is calculated as

$$v_A = \frac{B}{\sqrt{4\pi m_p n_p}} = \left(\frac{2}{3\mathcal{B}} \right)^{1/2} v_K(r) = \frac{c}{\sqrt{3\mathcal{B}}} \left(\frac{r}{r_S} \right)^{-1/2}. \quad (34)$$

Throughout this paper, $\zeta = 0.1$ is adopted.

The second-order Fermi acceleration is limited by various processes. The proton-proton relaxation and Coulomb scattering, as seen in equations (20) and (21), are also possible processes to suppress such a stochastic acceleration. If the radiation energy is high enough to damp the magnetic turbulent waves by the Compton scattering, the Compton drag can prevent the protons from accelerating (Thompson & Blaes 1998). We approximate the timescale for the Compton drag as

$$t_{\text{Cd}} = \frac{B^2}{(4/3)\sigma_T n_p U_\gamma c} \max \left(1, \frac{1}{\tau_p} \right), \quad (35)$$

where $U_\gamma \sim Lt_{\text{inf}}/(4\pi r_p^3/3)$, with luminosity $L = \eta \dot{M}c^2$, is the radiation energy density. Note that η is the mass-to-energy conversion efficiency, which takes a different value for each phase.

The protons potentially escape from the acceleration region via spatial diffusion. For isotropic turbulence, the diffusion time of the protons is given by (Kimura et al. 2015),

$$t_{\text{diff}} = 9\zeta \frac{r}{c} \left(\frac{r_L}{r} \right)^{s-2} \gamma^{s-2}. \quad (36)$$

The proton synchrotron emission and inelastic pp processes are adopted as a promising cooling mechanism in the TDR. Respective cooling timescales are given by

$$t_{\text{sync}} = \frac{3}{4} \left(\frac{m_p}{m_e} \right)^3 \frac{m_e c^2}{c \sigma_T U_B} \frac{1}{\gamma} \quad (37)$$

and

$$t_{pp} = \frac{1}{n_p \sigma_{pp} c K_{pp}}, \quad (38)$$

where $U_B = B^2/(8\pi)$ and $K_{pp} \sim 0.5$ are the energy density of the magnetic fields and the proton inelasticity, respectively, and the total cross section of the pp process is represented by $\sigma_{pp} \simeq 10^{-27} \text{ cm}^2 [34.3 + 1.88 \log(E_p/1 \text{ TeV}) + 0.25 \log^2(E_p/1 \text{ TeV})][1 - (E_{pp,\text{thr}}/E_p)^4]^2$ for $E_p \geq E_{pp,\text{thr}}$. Here $E_p = \gamma m_p c^2$ is the proton energy and $E_{pp,\text{thr}} = 1.22 \text{ GeV}$ (Kelner et al. 2006). The $p\gamma$ cooling timescale is given by (Dermer et al. 1996)

$$t_{p\gamma} = \left[\frac{c}{2\gamma^2} \bar{\epsilon}_{\text{pk}} \Delta \bar{\epsilon}_{\text{pk}} \sigma_{\text{pk}} K_{\text{pk}} \int_{\bar{\epsilon}_{\text{pk}}/(2\gamma)}^{\infty} dE_\gamma \frac{N_\gamma(E_\gamma)}{E_\gamma^2} \right]^{-1}, \quad (39)$$

where $\bar{\epsilon}_{\text{pk}} \sim 0.3 \text{ GeV}$, $\sigma_{\text{pk}} \sim 5 \times 10^{-28} \text{ cm}^2$, $K_{\text{pk}} \sim 0.2$, and $\Delta \bar{\epsilon}_{\text{pk}} \sim 0.2 \text{ GeV}$.

For the highly optically thin region during the RIAF phase ($\tau_p = n_p \sigma_T r \sim 3.1 \times 10^{-2} (\alpha/0.1)^{-1} (m_*/M_\odot)^{1/6} (r_*/R_\odot)^{-1/2} (r/r_p)^{-1/2} (\beta/1)^{1/2} (\dot{m}/0.01) (M_{\text{bh}}/10^7 M_\odot)^{1/3}$), the photon-proton interaction is by definition inefficient. Therefore, $t_{p\gamma}$ is much longer than the timescales by the other interactions. We neglect the effect of cooling by the photon-proton interaction for the RIAF phase (see Kimura et al. 2015 for the energy dependence of $t_{p\gamma}$ for the RIAFs in the low-luminosity AGNs).

By using equations (33) and (38), we obtain the Lorenz factor of the proton at

$t_{\text{accl}} = t_{pp}$:

$$\gamma_{pp}(r) = \left(\frac{\zeta}{K_{pp}}\right)^{1/(2-s)} \left(\frac{v_A}{c}\right)^6 \left(\frac{r}{r_L}\right) \left(\frac{1}{n_p \sigma_{pp} r}\right)^{1/(2-s)}. \quad (40)$$

This is estimated at $r = r_c$ to be

$$\begin{aligned} \gamma_{pp}(r_c) &\sim 1.2 \times 10^{-11} \left(\frac{\zeta}{0.1}\right)^3 \left(\frac{\mathcal{B}}{3}\right)^{-7/2} \left(\frac{\beta}{1.0}\right)^{33/2} \left(\frac{\dot{m}}{\dot{m}_{\text{fb}}}\right)^{-5/2} \\ &\times \left(\frac{M_{\text{bh}}}{10^7 M_\odot}\right)^{73/12} \left(\frac{m_*}{M_\odot}\right)^{41/12} \left(\frac{r_*}{R_\odot}\right)^{-31/4}, \end{aligned} \quad (41)$$

where we adopt $s = 5/3$ and $\sigma_{pp} \approx 3.6 \times 10^{-26} \text{ cm}^2$. Hence $\gamma_{pp}(r_c)$ cannot be larger than unity because of very efficient proton-proton cooling. Figure 1 shows the dependence of the characteristic cooling timescales normalized by t_{accl} on the proton energy. Each panel shows the normalized timescales of possible sites to produce the high-energy particles. Panel (a) depicts the normalized timescales of the first shock of the debris circularization phase of TDEs. The details of the other panels are described in the later corresponding sections. We note from panel (a) that the first (strongest) shock during the debris circularization is unlikely to produce the protons and neutrinos in the reasonable energy range, since the proton-proton collision cooling time is much shorter than the acceleration time.

2.2. Super-Eddington accretion phase

In an optically and geometrically thick accretion flow with the mass accretion rate exceeding the Eddington limit, the photons are trapped and restored as an entropy in the accreting gas without being radiated away. In other words, the advective cooling dominates the radiative cooling. The photon trapping radius is given by equating the radiative diffusion timescale with the accretion timescale as

$$\frac{r_{\text{trap}}}{r_S} = \frac{3}{2} \dot{m} \left(\frac{H}{r}\right) \sim 64 \left(\frac{H/r}{1.0}\right) \left(\frac{\dot{m}}{\dot{m}_{\text{fb}}}\right) \left(\frac{M_{\text{bh}}}{10^7 M_\odot}\right)^{-3/2} \left(\frac{m_*}{M_\odot}\right)^2 \left(\frac{r_*}{R_\odot}\right)^{-3/2}$$

with equation (28). As far as $\dot{m} \gg 1$, one can see $r_{\text{trap}} \gg r_t$ for $H/r \sim 1$ so that the TDE disk should be the super-Eddington accretion flow.

In the TDE context, we estimate the number density of the super-Eddington disk as

$$n_p = \frac{\dot{M}}{2\pi r^2 v_r m_p} \sim 2.7 \times 10^{13} \text{ cm}^{-3} \times \left(\frac{\alpha}{0.1}\right)^{-1} \left(\frac{\beta}{1.0}\right)^{3/2} \left(\frac{\dot{m}}{\dot{m}_{\text{fb}}}\right) \left(\frac{M_{\text{bh}}}{10^7 M_\odot}\right)^{-3/2} \left(\frac{m_*}{M_\odot}\right)^{5/2} \left(\frac{r_*}{R_\odot}\right)^{-3} \left(\frac{r}{r_p}\right)^{-3/2} \quad (42)$$

by using equation (28), where $v_r = \alpha v_K(r)$ is the radial drift velocity, which corresponds to that of the simplest solution for the slim-disk model (Abramowicz et al. 1988; Wang & Zhou 1999; Watarai 2006). From equation (40), the Lorentz factor γ_{pp} at the pericenter radius $r = r_p$ is estimated to be

$$\gamma_{pp}(r_p) \sim 1.6 \times 10 \left(\frac{\alpha}{0.1}\right)^3 \left(\frac{\zeta}{0.1}\right)^3 \left(\frac{\mathcal{B}}{3}\right)^{-7/2} \left(\frac{\beta}{1.0}\right)^{7/4} \times \left(\frac{\dot{m}}{\dot{m}_{\text{fb}}}\right)^{-5/2} \left(\frac{M_{\text{bh}}}{10^7 M_\odot}\right)^{65/12} \left(\frac{m_*}{M_\odot}\right)^{-53/12} \left(\frac{r_*}{R_\odot}\right)^{2/3}, \quad (43)$$

where $s = 5/3$ and $\sigma_{pp} \approx 3.6 \times 10^{-26} \text{ cm}^2$ are adopted. Taking account of the equipartition assumption of the magnetic field (see equation 31), we find $\gamma_{pp}(r) \propto B^7 \propto T^{7/2}$ together with $T \sim 10^{11} \text{ K}$ with $M_{\text{bh}} = 10^7 M_\odot$ and $\mathcal{B} = 3$. However, the disk temperature of the super-Eddington accretion flow increases up to $\sim 10^{8-9} \text{ K}$ by the latest three-dimensional radiation magneto-hydrodynamic (MHD) simulations of super-Eddington accretion flow around the SMBH with $M_{\text{bh}} = 5.0 \times 10^8 M_\odot$ (Jiang, Stone & Davis 2017). Since the disk temperature becomes lower as the black hole mass becomes lower, $\gamma_{pp}(r_p)$ cannot be larger than unity for $M_{\text{bh}} \lesssim 10^8 M_\odot$. This suggests that the cooling by the proton-proton collision is very efficient in the super-Eddington accretion flow. Panel (b) of Figure 1 depicts the dependence of characteristic timescales normalized by t_{accl} on the proton energy in the super-Eddington accretion flow. From the figure, the super-Eddington accretion flows are unlikely to accelerate the protons to the ultrarelativistic regime and thus produce the neutrinos in the reasonable energy range.

2.3. Radiatively inefficient accretion flow phase

The RIAFs are very hot and optically thin so that they can produce high-energy emissions. This is because a heat produced via turbulent viscosity is stored as entropy and transported inwardly with accretion. The original model of the RIAF is a one-dimensional, optically thin, advection-dominated accretion flow (ADAF) (Narayan & Yi 1994, 1995).

The number density of the RIAFs is estimated to be

$$n_p = \frac{\dot{M}}{2\pi\alpha r^2 v_K m_p} \sim 3.2 \times 10^9 \text{ cm}^{-3} \\ \times \left(\frac{\alpha}{0.1}\right)^{-1} \left(\frac{\beta}{1.0}\right)^{3/2} \left(\frac{\dot{m}}{0.01}\right) \left(\frac{m_*}{M_\odot}\right)^{1/2} \left(\frac{r_*}{R_\odot}\right)^{-3/2} \left(\frac{r}{r_p}\right)^{3/2}, \quad (44)$$

where the radial velocity is assumed to be αv_K as a simplest solution of the ADAF.

Substituting equations (30), (31), (34), and (44) into equation (40), the Lorenz factor at $t_{pp} = t_{\text{accel}}$ during the RIAF phase is estimated to be

$$\gamma_{pp}(r_p) \sim 1.1 \times 10^{11} \left(\frac{\zeta}{0.1}\right)^3 \left(\frac{\mathcal{B}}{3}\right)^{-7/2} \left(\frac{\alpha}{0.1}\right)^{5/2} \left(\frac{\beta}{1.0}\right)^{7/4} \left(\frac{\dot{m}}{0.01}\right)^{-5/2} \\ \times \left(\frac{M_{\text{bh}}}{10^7 M_\odot}\right)^{5/3} \left(\frac{m_*}{M_\odot}\right)^{7/12} \left(\frac{r_*}{R_\odot}\right)^{-7/4}, \quad (45)$$

where $s = 5/3$ and $\sigma_{pp} \approx 3.6 \times 10^{-26} \text{ cm}^2$ are adopted. By using equations (33) and (36), we obtain the Lorenz factor at $t_{\text{diff}} = t_{\text{accel}}$:

$$\gamma_{\text{diff}}(r) = \left(3\zeta \frac{v_A}{c}\right)^{1/(2-s)} \left(\frac{r}{r_L}\right). \quad (46)$$

Substituting equations (30), (31), (34), and (44) into equations (33) and (36), this is estimated at $r = r_p$ to be

$$\gamma_{\text{diff}}(r_p) \sim 4.8 \times 10^5 \left(\frac{\alpha}{0.1}\right)^{-1/2} \left(\frac{\zeta}{0.1}\right)^3 \left(\frac{\mathcal{B}}{3}\right)^{-2} \left(\frac{\dot{m}}{0.01}\right)^{1/2} \left(\frac{\beta}{1.0}\right)^{7/4} \\ \times \left(\frac{M_{\text{bh}}}{10^7 M_\odot}\right)^{5/3} \left(\frac{r}{r_p}\right)^{-7/4} \left(\frac{m_*}{M_\odot}\right)^{7/12} \left(\frac{r_*}{R_\odot}\right)^{-7/4}, \quad (47)$$

where $s = 5/3$ and $\sigma_{pp} \approx 3.6 \times 10^{-26} \text{ cm}^2$ are adopted. Panel (d) of Figure 1 depicts the dependence of characteristic timescales normalized by t_{accl} on the proton energy in the RIAF. We note from the figure that the diffusion timescale is the shortest among the timescales of the other mechanisms, which prevents the protons from accelerating. In this case, the protons can be accelerated up to $E_{p,\text{diff}} = \gamma_{\text{diff}}(r_p) m_p c^2 \simeq 0.45 \text{ PeV}$.

2.4. Magnetically Arrested Disks

A large-scale poloidal magnetic field prevents gas from accreting continuously at a magnetospheric radius, which is far outside the event horizon of the black hole (Bisnovatyi-Kogan & Ruzmaikin 1974). Around the magnetospheric radius, the gas flow breaks up into a blob-like stream and moves inward by diffusing via magnetic interchanges through the magnetic field. Narayan, Igumenshchev & Abramowicz (2003) called such a disrupted accretion flow a magnetically arrested disk (MAD). The MAD state has been tested by numerical MHD simulations (McKinney, Tchekhovskoy & Blandford 2012; McKinney, Dai & Avara 2015; Marshall, Avara & McKinney 2018).

The main difference from the previous two cases is how to estimate the strength of the magnetic field. By equating the gravitational force per unit area of the radially accreting mass $GM\rho_{p,\text{MAD}}H/r^2$ with the magnetic energy density $B^2/(8\pi)$, the square of the magnetic field strength of the MAD state is then given by

$$B_{\text{MAD}}^2 = 2\sqrt{2}\pi \left(\frac{\alpha}{\epsilon}\right) \left(\frac{H}{r}\right) \rho_p v_{\text{ff}}^2(r), \quad (48)$$

where $v_{\text{ff}}(r) = \sqrt{2GM_{\text{bh}}/r}$ is the freefall velocity and the mass conservation law gives the local density estimated at the magnetosphere as $\rho_{p,\text{MAD}} = (v_r/v_{r,\text{MAD}})\rho_p$ with the radial magnetic diffusion velocity $v_{r,\text{MAD}} = \epsilon v_{\text{ff}}(r)$ with $\epsilon \lesssim 0.01$ (Narayan, Igumenshchev & Abramowicz 2003). Comparing with equation (31), we

obtain $B_{\text{MAD}}^2/B^2 = (3/\sqrt{2})\mathcal{B}(\alpha/\epsilon)(H/r)$. Since $H/r \sim 1$ for the super-Eddington accretion flows and RIAFs, the field strength in the MAD state is $\sim \sqrt{\alpha/\epsilon}$ times larger than that of the dipole field for the given plasma beta.

2.4.1. Super-Eddington Magnetically Arrested Disks

Here we apply the MAD state for the super-Eddington accretion flow. The number density of the super-Eddington MAD is given by

$$n_{p,\text{MAD}} = \frac{\dot{M}}{2\pi r^2 v_{r,\text{MAD}} m_p} \sim 1.9 \times 10^{14} \text{ cm}^{-3} \left(\frac{\epsilon}{0.01}\right)^{-1} \left(\frac{M_{\text{bh}}}{10^7 M_\odot}\right)^{-3/2} \times \left(\frac{\beta}{1.0}\right)^{3/2} \left(\frac{\dot{m}}{\dot{m}_{\text{fb}}}\right) \left(\frac{m_*}{M_\odot}\right)^{5/2} \left(\frac{r_*}{R_\odot}\right)^{-3} \left(\frac{r}{r_p}\right)^{-3/2} \quad (49)$$

by using equation (28). By substituting equation (49) into equation (48), we estimate B_{MAD} at $r = r_p$ for $H/r \sim 1$ as

$$B_{\text{MAD}}(r_p) \sim 2.2 \times 10^6 \text{ Gauss} \left(\frac{\epsilon}{0.01}\right)^{-1/2} \left(\frac{M_{\text{bh}}}{10^7 M_\odot}\right)^{-5/12} \times \left(\frac{\beta}{1.0}\right)^{5/4} \left(\frac{\dot{m}}{\dot{m}_{\text{fb}}}\right)^{1/2} \left(\frac{m_*}{M_\odot}\right)^{17/12} \left(\frac{r_*}{R_\odot}\right)^{-2}. \quad (50)$$

Panel (e) of Figure 1 depicts the dependence of characteristic timescales normalized by t_{accl} on the proton energy in the super-Eddington MAD state. We note from the figure that the Compton drag is the most efficient mechanism to prevent the protons from accelerating. By using equations (33) and (35), we obtain the Lorentz factor of the proton at $t_{\text{accl}} = t_{\text{Cd}}$:

$$\gamma_{\text{Cd}}(r) = \left(\frac{\epsilon \zeta}{\eta \tau_p}\right)^{1/(2-s)} \left(\frac{v_A}{c}\right)^{2/(2-s)} \left(\frac{r}{r_L}\right) \left(\frac{B^2 r^3 v_{\text{ff}}}{\dot{M} c^2 r}\right)^{1/(2-s)}. \quad (51)$$

It is estimated at $r = r_p$ to be

$$\gamma_{\text{Cd}}(r_p) \sim 2.6 \left(\frac{\epsilon}{0.01}\right)^{5/2} \left(\frac{\eta_{\text{MAD}}}{0.15}\right)^{-3} \left(\frac{\zeta}{0.1}\right)^3 \left(\frac{\beta}{1.0}\right)^{19/4} \left(\frac{M_{\text{bh}}}{10^7 M_\odot}\right)^{89/12} \times \left(\frac{\dot{m}}{\dot{m}_{\text{fb}}}\right)^{-5/2} \left(\frac{m_*}{M_\odot}\right)^{-41/12} \left(\frac{r_*}{R_\odot}\right)^{-1}, \quad (52)$$

where we adopt $s = 5/3$ as the spectral index and $\eta_{\text{MAD}} = 0.15$ as the radiative efficiency, which is obtained from three-dimensional general relativistic radiation MHD simulations (McKinney, Dai & Avara 2015). The second efficient mechanism is the proton-proton cooling. From equation (40) with equation (48), γ_{pp} is estimated at $r = r_p$ to be

$$\begin{aligned} \gamma_{pp}(r_p) &\sim 2.3 \times 10^2 \left(\frac{\epsilon}{0.01}\right)^{5/2} \left(\frac{\dot{m}}{\dot{m}_{\text{fb}}}\right)^{-5/2} \left(\frac{M_{\text{bh}}}{10^7 M_{\odot}}\right)^{65/12} \\ &\times \left(\frac{\zeta}{0.1}\right)^3 \left(\frac{\beta}{1.0}\right)^{7/4} \left(\frac{m_*}{M_{\odot}}\right)^{-53/12} \left(\frac{r_*}{R_{\odot}}\right)^2, \end{aligned} \quad (53)$$

where $s = 5/3$ and $\sigma_{pp} \approx 3.6 \times 10^{-26} \text{ cm}^2$ are adopted. The third efficient mechanism is the synchrotron cooling. By using equations (33) and (37), we obtain the Lorenz factor of the proton at $t_{\text{accl}} = t_{\text{sync}}$:

$$\gamma_{\text{sync}}(r) = \left(\frac{3}{4}\zeta\right)^{1/(3-s)} \left(\frac{m_p}{m_e}\right)^{2/(3-s)} \left(\frac{m_p c^2}{r \sigma_{\text{T}} U_{\text{B}}}\right)^{1/(3-s)} \left(\frac{v_{\text{A}}}{c}\right)^{2/(3-s)} \left(\frac{r}{r_{\text{L}}}\right)^{(2-s)/(3-s)}. \quad (54)$$

It is estimated at $r = r_p$ to be

$$\begin{aligned} \gamma_{\text{sync}}(r_p) &\sim 9.4 \times 10^4 \left(\frac{\epsilon}{0.01}\right)^{5/8} \left(\frac{\zeta}{0.1}\right)^{3/4} \left(\frac{\beta}{1.0}\right)^{-5/16} \left(\frac{M_{\text{bh}}}{10^7 M_{\odot}}\right)^{41/48} \\ &\times \left(\frac{\dot{m}}{\dot{m}_{\text{fb}}}\right)^{-5/8} \left(\frac{m_*}{M_{\odot}}\right)^{-65/48} \left(\frac{r_*}{R_{\odot}}\right)^{5/4}, \end{aligned} \quad (55)$$

where $s = 5/3$ is adopted.

It is clear from equation (52) that the protons can be accelerated to at most $\sim 2.6 \text{ GeV}$ if $M_{\text{bh}} \leq 10^7 M_{\odot}$. We find from the above three equations that γ_{Cd} and γ_{pp} rapidly increase with the black hole mass, whereas γ_{sync} weakly depends on it. We also find that $\gamma_{\text{Cd}} \lesssim \gamma_{pp}$ for $M_{\text{bh}} \lesssim 10^8 M_{\odot}$, meaning the Compton drag is more efficient than the proton-proton cooling in the given mass range. Next we compare γ_{Cd} with γ_{sync} . The synchrotron cooling timescale is shorter than the Compton drag timescale if $\gamma_{\text{Cd}}/\gamma_{\text{sync}} > 1$. Because we find from equations (52) and (55) that $\gamma_{\text{Cd}}/\gamma_{\text{sync}} \propto M_{\text{bh}}^{105/16}$, there is a critical value of black hole mass, $M_{\text{bh}} \sim 10^{7.7} M_{\odot}$, where $\gamma_{\text{Cd}}/\gamma_{\text{sync}} = 1$. Therefore, the Compton drag is more efficient

than the synchrotron cooling if $M_{\text{bh}} < 10^{7.7} M_{\odot}$. In this case, the protons can be accelerated to $E_{p,\text{Cd}} = \gamma_{\text{Cd}}(r_{\text{p}}) m_{\text{p}} c^2 \simeq 2.2 \text{ TeV} (M_{\text{bh}}/10^{7.4} M_{\odot})^{89/12}$. On the other hand, the synchrotron cooling is more efficient if $M_{\text{bh}} \gtrsim 10^{7.7} M_{\odot}$. In this case, the protons can be accelerated up to $E_{p,\text{sync}} = \gamma_{\text{sync}}(r_{\text{p}}) m_{\text{p}} c^2 \simeq 0.35 \text{ PeV} (M_{\text{bh}}/10^{7.7} M_{\odot})^{41/48}$.

2.4.2. Radiatively Inefficient Magnetically Arrested Disks

Next we consider the RIAF with the MAD state. We call it "radiatively inefficient MAD" in what follows. The number density of the radiatively inefficient MAD is given by

$$n_{p,\text{MAD}} = \frac{\dot{M}}{2\pi r^2 v_{r,\text{MAD}} m_{\text{p}}} \sim 2.2 \times 10^{10} \text{ cm}^{-3} \left(\frac{\epsilon}{0.01}\right)^{-1} \left(\frac{\dot{m}}{0.01}\right) \left(\frac{r}{r_{\text{p}}}\right)^{-3/2} \\ \times \left(\frac{\beta}{1.0}\right)^{3/2} \left(\frac{m_*}{M_{\odot}}\right)^{1/2} \left(\frac{r_*}{R_{\odot}}\right)^{-3/2}, \quad (56)$$

where equation (13) is used for \dot{M} . We confirm that the radiatively inefficient MAD is optically thin because of $\tau_{\text{p}} = n_{p,\text{MAD}} \sigma_{\text{T}} r \sim 2.2 \times 10^{-1} (\epsilon/0.01)^{-1} (\dot{m}/0.01) (M_{\text{bh}}/10^7 M_{\odot})^{1/3} (r/r_{\text{p}})^{-1/2} (\beta/1.0)^{1/2} (r/R_{\odot})^{1/2}$. By substituting equation (56) into equation (48), we estimate the magnetic field strength at $r = r_{\text{p}}$ for $H/r \sim 1$ as

$$B_{\text{MAD}}(r_{\text{p}}) \sim 9.1 \times 10^3 \text{ G} \left(\frac{\epsilon}{0.01}\right)^{-1/2} \left(\frac{\alpha}{0.1}\right)^{1/2} \left(\frac{\beta}{1.0}\right)^{5/4} \left(\frac{\dot{m}}{0.01}\right)^{1/2} \left(\frac{M_{\text{bh}}}{10^7 M_{\odot}}\right)^{1/3} \\ \times \left(\frac{m_*}{M_{\odot}}\right)^{5/12} \left(\frac{r_*}{R_{\odot}}\right)^{-5/4} \quad (57)$$

Panel (f) of Figure 1 depicts the dependence of characteristic timescales normalized by t_{accl} on the proton energy in the radiatively inefficient MAD state. We note from the figure that the synchrotron process is the dominant cooling mechanism. From equation (54), we can estimate the Lorentz factor at $t_{\text{accl}} = t_{\text{sync}}$ as

$$\gamma_{\text{sync}}(r_{\text{p}}) \sim 2.7 \times 10^7 \left(\frac{\epsilon}{0.01}\right)^{5/8} \left(\frac{\zeta}{0.1}\right)^{3/4} \left(\frac{\beta}{1.0}\right)^{-5/16} \left(\frac{M_{\text{bh}}}{10^7 M_{\odot}}\right)^{-1/12} \\ \times \left(\frac{\dot{m}}{0.01}\right)^{-5/8} \left(\frac{m_*}{M_{\odot}}\right)^{-5/48} \left(\frac{r_*}{R_{\odot}}\right)^{5/16}, \quad (58)$$

where $s = 5/3$ is adopted. The protons can be accelerated up to $E_{p,\text{sync}} = \gamma_{\text{sync}} m_p c^2 \simeq 25 \text{ PeV}$.

3. Neutrino Spectra and Luminosities

The bolometric luminosity of the protons is defined by

$$L_p \equiv \int dV \int dp \frac{4\pi p^3 F(p) c}{t_{\text{diff}}}, \quad (59)$$

where $dV = 4\pi r^2 dr$ because the disk is assumed to be a spherically symmetric, t_{diff} is the shortest time when the acceleration is prevented in the RIAF phase, and $F(p)$ is the distribution function of the nonthermal protons. According to Becker et al. (2006), $F(p)$ is given by

$$F(p) = \begin{cases} A_l E_p^{-(1+s)} & E_p < E_{p,\text{diff}} \\ A_h E_p^{-3/2} \exp[-(E_p/E_{p,\text{diff}})^{2-s}/(2-s)] & E_p \gtrsim E_{p,\text{diff}}, \end{cases} \quad (60)$$

where A_l and A_h are the normalization coefficients and $A_l/A_h = E_{p,\text{diff}}^{(2s-1)/2}/e^3$ at $E_p = E_{p,\text{diff}}$.

By substituting equations (36) and (60) into equation (59) with the assumption that

$L_p = \eta_{\text{cr}} \dot{M} c^2$, A_l is determined to be

$$A_l = \frac{(5-2s)(10-s)}{64\pi^2} \left(\frac{c}{r_d}\right)^3 E_{p,\text{diff}}^{s-3} t_{\text{diff}}(r_d, \gamma_{\text{diff}}) \eta_{\text{cr}} \dot{M} c^2,$$

where η_{cr} is the injection efficiency for the protons, and we use $\eta_{\text{cr}} = 0.1$ as a fiducial value unless otherwise noted. Similarly, A_h is estimated to be

$$A_h = \frac{(5-2s)(10-s)}{64\pi^2 e^3} \left(\frac{c}{r_d}\right)^3 E_{p,\text{diff}}^{-5/2} t_{\text{diff}}(r_d, \gamma_{\text{diff}}) \eta_{\text{cr}} \dot{M} c^2,$$

where $t_{\text{diff}}(r, \gamma_{\text{diff}}) \sim 10^4 \text{ s } (\mathcal{B}/3)^{1/2} (r/r_d)^{3/2} (M_{\text{bh}}/10^7 M_\odot)^{-1/2}$ with $\sigma_{pp} \approx 3.6 \times 10^{-26} \text{ cm}^2$.

The differential luminosity of the protons is estimated to be

$$E_p L_{E_p} = \int dV \frac{4\pi p^3 F(p) E_p}{t_{\text{diff}}} = (5-2s) \eta_{\text{cr}} \dot{M} c^2$$

$$\times \begin{cases} (E_p/E_{p,\text{diff}})^{5-2s} & E_p \lesssim E_{p,\text{diff}} \\ (E_p/E_{p,\text{diff}})^{9/2-s} \exp[(1 - (E_p/E_{p,\text{diff}})^{2-s})/(2-s)] & E_p \gtrsim E_{p,\text{diff}}. \end{cases} \quad (61)$$

The corresponding spectra of the neutrinos are defined by

$$\begin{aligned} E_\nu L_{E_\nu} &= \int dV \frac{4\pi p^3 F(p) E_p}{t_{pp}} = \eta_{\text{cr}} \dot{M} c^2 \times \frac{t_{\text{diff}}}{t_{pp}} \times \frac{(10-s)(5-2s)}{2} \\ &\times \begin{cases} (E_\nu/E_{\nu,\text{diff}})^{3-s} & E_\nu \lesssim E_{\nu,\text{diff}} \\ (E_\nu/E_{\nu,\text{diff}})^{5/2} \exp[(1 - (E_\nu/E_{\nu,\text{diff}})^{2-s})/(2-s)] & E_\nu \gtrsim E_{\nu,\text{diff}}, \end{cases} \end{aligned} \quad (62)$$

where $E_\nu = 0.05E_p$ (thus $E_{\nu,\text{diff}} = 0.05E_{p,\text{diff}}$) and the ratio of diffusion to proton-proton collision timescales is

$$\frac{t_{\text{diff}}}{t_{pp}} = \frac{9}{2} \zeta n_p \sigma_{pp} r^{3-s} \left(\frac{r_L}{m_p c^2} \right)^{s-2} \left(\frac{E_p}{E_{p,\text{diff}}} \right)^{s-2} E_{p,\text{diff}}^{s-2}.$$

By adopting $s = 5/3$ and $\sigma_{pp} \approx 3.6 \times 10^{-26} \text{ cm}^2$, we obtain $t_{\text{diff}}/t_{pp} \sim 1.7 \times 10^{-2} (\alpha/0.1)^{-1} (\mathcal{B}/3)^{1/2} (\dot{m}/0.01) (E_\nu/E_{\nu,\text{diff}})^{-1/3}$. By differentiating equations (61) and (62), the energy of protons and neutrinos at the peak of the spectra is given by $E_{p,\text{pk}} = (4913/216)E_{p,\text{diff}}$ and $E_{\nu,\text{pk}} = (125/8)E_{\nu,\text{diff}}$, respectively. The differential luminosity of the protons at the peak is then given by

$$\begin{aligned} E_p L_{E_p}|_{\text{pk}} &= (5-2s)\eta_{\text{cr}} \dot{M} c^2 \left(\frac{E_{p,\text{pk}}}{E_{p,\text{diff}}} \right)^{9/2-s} \exp \left[\frac{1}{2-s} \left(1 - \left(\frac{E_{p,\text{pk}}}{E_{p,\text{diff}}} \right)^{2-s} \right) \right] \\ &= g_p(s) \eta_{\text{cr}} M_{\text{bh}} \dot{m} \\ &\propto t^{-5/3}, \end{aligned} \quad (63)$$

where $g_p(s) = (5-2s)(E_{p,\text{pk}}/E_{p,\text{diff}})^{9/2-s} \exp[(1 - (E_{p,\text{pk}}/E_{p,\text{diff}})^{2-s})/(2-s)]$. Similarly, the differential luminosity of the neutrinos at the peak is given by

$$\begin{aligned} E_\nu L_{E_\nu}|_{\text{pk}} &= \frac{(10-s)(5-2s)\eta_{\text{cr}} \dot{M} c^2}{2} \left(\frac{E_{\nu,\text{pk}}}{E_{\nu,\text{diff}}} \right)^{5/2} \exp \left[\frac{1}{2-s} \left(1 - \left(\frac{E_{\nu,\text{pk}}}{E_{\nu,\text{diff}}} \right)^{2-s} \right) \right] \\ &\times \left. \frac{t_{\text{diff}}}{t_{pp}} \right|_{\gamma=\gamma_{\text{pk}}} \\ &\propto g_\nu(s) \eta_{\text{cr}} \alpha^{-1} \mathcal{B}^{1/2} M_{\text{bh}} \dot{m}^2 \\ &\propto t^{-10/3}, \end{aligned} \quad (64)$$

where $g_\nu(s) = (10 - s)(5 - 2s)(E_{\nu,\text{pk}}/E_{\nu,\text{diff}})^{5/2} \exp[(1 - (E_{\nu,\text{pk}}/E_{\nu,\text{diff}})^{2-s})/(2 - s)]/2$.

The neutrino energy emitted at the peak is estimated as $E_{\nu,\text{pk}} = (25/32)E_{p,\text{diff}} \simeq 0.35 \text{ PeV } (M_{\text{bh}}/10^7 M_\odot)^{5/3}$ with the other given appropriate parameters.

The gamma-ray photons are also produced by pionic decay with $E_{\gamma,\text{pk}} = (25/16)E_{p,\text{diff}} \sim 0.7 \text{ PeV}$. They naturally cause the pair production by the interaction with the photons having the larger energy than $E_{\text{rad}} = (m_e c^2)^2/E_{\gamma,\text{pk}} \sim 3.7 \times 10^{-4} \text{ eV}$. The optical depth is estimated to be $\tau_\gamma \sim \sigma_{\text{T}}(t_{\text{inf}}L_{\text{rad}}/E_{\text{rad}})/(\pi r_p^2) \sim 2.5 \times 10^4$, where $L_{\text{rad}} \sim 10^{36} \text{ erg/s}$ is adopted as the radio luminosity of the ADAF model (e.g. see Figure 1 of Kimura et al. 2015). Since the gamma-ray photons cause the pair production very efficiently because of $\tau_\gamma \gg 1$, the gamma-ray emission is unlikely to be observed during the RIAF phase.

Next, for the MAD state, the synchrotron radiation can be dominant among the other cooling processes because of the stronger magnetic field than the non-MAD case. In this case, the bolometric luminosity of the accelerated protons is given by

$$L_p = \int dV \int dp \frac{4\pi p^3 F_{\text{sync}}(p) c}{t_{\text{sync}}}, \quad (65)$$

where the distribution function of protons, $F_{\text{sync}}(p)$, for the synchrotron cooling case is given by Stawarz & Petrosian (2008) as

$$F_{\text{sync}}(p) = A_s \left(\frac{E_p}{c}\right)^2 \exp\left[-\frac{1}{3-s} \left(\frac{E_p}{E_{p,\text{sync}}}\right)^{3-s}\right] \quad (66)$$

with the normalization coefficient A_s for the entire energy range. By substituting equations (37) and (66) into equation (65) with the assumption that $L_p = \eta_{\text{cr}} \dot{M} c^2$, A_s is determined as

$$A_s = \frac{1}{32\pi^2} \frac{1}{g_s(s)} \left(\frac{c}{r_d}\right)^3 \frac{c^2}{E_{p,\text{sync}}^6} t_{\text{sync}}(r_d, \gamma_{\text{sync}}(r_d)) \eta_{\text{cr}} \dot{M} c^2, \quad (67)$$

where $g_s(s) \equiv \int_0^\infty x^6 \exp[-x^{1/(3-s)}/(3-s)] dx$ and $g_s(5/3) \simeq 120$.

The differential luminosity of the protons is estimated to be

$$E_p L_{E_p} = \int dV \frac{4\pi p^3 F_{\text{sync}}(p) E_p}{t_{\text{sync}}} = \frac{\eta_{\text{cr}} \dot{M} c^2}{g_s(s)} \left(\frac{E_p}{E_{p,\text{sync}}}\right)^7 \exp\left[\frac{-1}{3-s} \left(\frac{E_p}{E_{p,\text{sync}}}\right)^{3-s}\right] \quad (68)$$

for the entire energy range. The corresponding spectra of the neutrinos are defined by

$$E_\nu L_{E_\nu} \simeq \int dV \frac{4\pi p^3 F_{\text{sync}}(p) E_p}{t_{pp}} = \frac{\eta_{\text{cr}} \dot{M} c^2}{3g_s(s)} \left(\frac{E_p}{E_{p,\text{sync}}} \right)^6 \exp \left[\frac{-1}{3-s} \left(\frac{E_p}{E_{p,\text{sync}}} \right)^{3-s} \right] \times \frac{t_{\text{sync}}(r_d, \gamma_{\text{sync}}(r_d))}{t_{pp}(r_d)}, \quad (69)$$

where the ratio of synchrotron cooling to proton-proton collision timescales is given by

$$\frac{t_{\text{sync}}(r_d, \gamma_{\text{sync}})}{t_{pp}(r_d)} = \frac{3}{4} K_{pp} \epsilon \left(\frac{m_p}{m_e} \right)^2 \left(\frac{v_K(r_d)}{c} \right)^{-2} \frac{\sigma_{pp}}{\sigma_T} \left(\frac{H}{r} \right)^{-1} \frac{1}{\gamma_{\text{sync}}(r_d)}. \quad (70)$$

By differentiating equations (68) and (69), the energy of the protons and neutrinos at the peak of the spectra is given by $E_{p,\text{pk}} = 6^{3/4} E_{p,\text{sync}}$ and $E_{\nu,\text{pk}} = (6^{3/4}/20) E_{p,\text{sync}}$, respectively.

The differential luminosity of the protons at the peak is given by

$$E_p L_{E_p}|_{\text{pk}} = \frac{\eta_{\text{cr}}}{g_s(s)} \left(\frac{E_{p,\text{pk}}}{E_{p,\text{sync}}} \right)^6 \exp \left[-\frac{1}{3-s} \left(\frac{E_{p,\text{pk}}}{E_{p,\text{sync}}} \right)^{3-s} \right] \dot{M} c^2 \propto M_{\text{bh}} \dot{m} \propto t^{-5/3}. \quad (71)$$

Similarly, the neutrino luminosity at the peak is given by

$$E_\nu L_{E_\nu}|_{\text{pk}} = \frac{1}{3} \frac{\eta_{\text{cr}}}{g_s(s)} \left(\frac{E_{\nu,\text{pk}}}{E_{p,\text{sync}}} \right)^6 \exp \left[-\frac{1}{3-s} \left(\frac{E_{\nu,\text{pk}}}{E_{p,\text{sync}}} \right)^{3-s} \right] \dot{M} c^2 \times \frac{t_{\text{sync}}(r_d, \gamma_{\text{sync}})}{t_{pp}(r_d)} \propto \gamma_{\text{sync}}^{-1} \mathcal{B} M_{\text{bh}} \dot{m} \propto \zeta^{1/(s-3)} \epsilon^{(2-s)/(6-2s)} \alpha^{1/(s-3)} M_{\text{bh}}^{(8-s)/(12-4s)} r_d^{-s/(12-4s)} \dot{m}^{(6-s)/(6-2s)} \propto t^{-(5/6)(6-s)/(3-s)}. \quad (72)$$

For $s = 5/3$, $E_\nu L_{E_\nu}|_{\text{pk}}$ is proportional to $t^{-65/24}$. This is steeper than the standard decay rate. For the super-Eddington MAD state, the neutrino energy at the peak is calculated to be $E_{\nu,\text{pk}} = 6^{3/4} E_{p,\text{sync}} \simeq 80 \text{ TeV} (M_{\text{bh}}/10^7 M_\odot)^{41/48}$ with the other given appropriate parameters. As discussed in the last paragraph of Section 2.4.1, the Compton drag is the most efficient mechanism to prevent the protons from accelerating in the super-Eddington MAD if $M_{\text{bh}} \lesssim 10^{7.7} M_\odot$. In this case, $E_\nu L_{E_\nu} \simeq \int dV 4\pi p^3 F_{\text{Cd}}(p) E_p / t_{pp}$,

where $F_{\text{Cd}}(p) \propto p^2 \exp[-(E_p/E_{p,\text{Cd}})^{2-s}/(2-s)]$ is the distribution function of protons for the Compton drag (Stawarz & Petrosian 2008). The neutrino luminosity is then estimated as $E_\nu L_{E_\nu}|_{\text{pk}} \propto \eta_{\text{cr}} \dot{M} c^2 \propto t^{-5/3}$ at the peak of the neutrino energy $E_{\nu,\text{pk}} = (54/5) E_{p,\text{Cd}} \sim 24 \text{ TeV} (M_{\text{bh}}/10^{7.4} M_\odot)^{89/12}$. The optical depth for Thomson scattering is estimated to be $\tau_p = 2.9 \times 10^2 (\epsilon/0.01)^{-1} (\beta/1.0)^{1/2} (M_{\text{bh}}/10^{7.7} M_\odot)^{-7/6} (m_*/M_\odot)^{13/6} (r_*/R_\odot)^{-2} (\dot{m}/\dot{m}_{\text{fb}})(r/r_p)^{-1/2}$. Because it is much larger than unity, the super-Eddington MAD is highly opaque to gamma-ray photons produced by pionic decay.

For the radiatively inefficient MAD state, the neutrino energy at the peak is calculated to be $E_{\nu,\text{pk}} \simeq 4.8 \text{ PeV} (M_{\text{bh}}/10^7 M_\odot)^{-1/12}$ with the other given appropriate parameters. As well as what we discussed above for the case of the non-MAD state, the gamma-ray photons produced by pionic decay are unlikely to escape from the radiatively inefficient MAD because of the very efficient pair production.

Figure 2 shows the differential luminosity spectra of the protons and neutrinos. Panels (a)-(c) show the cases of the super-Eddington MAD state, the RIAF phase, and the radiatively inefficient MAD state, respectively. It is noted from the three panels that the neutrino emission has a nearly Eddington luminosity at the peak in the MAD state, while the neutrino emissions has $E_\nu L_{E_\nu} \sim 7.0 \times 10^{42} \text{ erg s}^{-1} (\eta_{\text{cr}}/0.1)$ at the peak in the RIAF case of the non-MAD state and $E_\nu L_{E_\nu} \sim 3.2 \times 10^{39} \text{ erg s}^{-1} (\eta_{\text{cr}}/0.1)$ at the peak in the RIAF case of the MAD state.

4. Discussion

In the MAD state, the magnetic field is so strong that the proton synchrotron radiation is efficient. Since the energy spectrum of the relativistic proton is very hard (see

equation 68), the typical photon energy is given by

$$\langle h\nu_{\text{sync}} \rangle = \frac{hq_e}{2\pi m_p c} B_{\text{MAD}}(r_p) \gamma_{\text{sync}}(r_p)^2 \sim 0.34 \text{ MeV} \left(\frac{B_{\text{MAD}}(r_p)}{1.2 \times 10^6 \text{ G}} \right) \left(\frac{\gamma_{\text{sync}}(r_p)}{4.5 \times 10^5} \right)^2, \quad (73)$$

where we use equations (50) and (54). Such photons can potentially become the target for $p\gamma$ cooling. Here we roughly estimate $t_{p\gamma}$ for such a case. Since $L_{E_p} \propto E_p^5$ from equation (68), we approximate the energy density of proton synchrotron photons as $U_\gamma(E_\gamma) \sim U_{\gamma,\text{pk}}(E_\gamma/\langle h\nu_{\text{sync}} \rangle)^3$ for $E_\gamma < \langle h\nu_{\text{sync}} \rangle$ and $U_\gamma(E_\gamma) \sim 0$ for $E_\gamma > \langle h\nu_{\text{sync}} \rangle$. For protons with energy $E_{p,\text{sync}} = \gamma_{\text{sync}}(r_p)m_p c^2$, almost all their energy is converted to the synchrotron emission which is the dominant cooling process, so that we can write $U_{\gamma,\text{pk}} \sim (r_p/c)L_p/\langle h\nu_{\text{sync}} \rangle V$, where $V \sim r_p^3$ is the volume of the emission region. Then the photon number spectrum is written as $N_\gamma(E_\gamma) \sim (U_{\gamma,\text{pk}}/\langle h\nu_{\text{sync}} \rangle)(E_\gamma/\langle h\nu_{\text{sync}} \rangle)^2$ for $E_\gamma < \langle h\nu_{\text{sync}} \rangle$. Substituting this into equation (39), we derive the $p\gamma$ cooling time for the protons as

$$t_{p\gamma}(\gamma) \sim 10^{-5} \text{ s } \gamma^2 \left(1 - \frac{\gamma_c}{\gamma} \right)^{-1} \left(\frac{\langle h\nu_{\text{sync}} \rangle}{0.1 \text{ MeV}} \right)^3 \left(\frac{L_p}{L_{\text{Edd}}} \right)^{-1} \left(\frac{r_p/c}{10^3 \text{ s}} \right)^{-1} \left(\frac{V}{10^{39} \text{ cm}^3} \right), \quad (74)$$

which is validated when $\gamma > \gamma_c = \bar{\epsilon}_{\text{pk}}/2\langle h\nu_{\text{sync}} \rangle \sim 500$. For protons with $\gamma < \gamma_c$, there are no target photons in their rest frame. Namely, if $\gamma \gg \gamma_c$, one can see $t_{p\gamma} \sim 10^5(\gamma/10^5)^2 \text{ s}$, which is much longer than the acceleration time t_{accl} . Therefore, the proton acceleration is not limited by the $p\gamma$ cooling.

The baryonic loading parameter is given by $\xi_{\text{bl}} = L_p/L_\gamma$, where $L_p = \eta_{\text{cr}} \dot{M}_{\text{fb}} c^2 \sim 2.4 \times 10^{45} \text{ erg s}^{-1} (\eta_{\text{cr}}/0.1) (M_{\text{bh}}/10^{7.7} M_\odot)^{-1/2} (m_*/M_\odot)^2 (r_*/R_\odot)^{-3/2} (t/t_{\text{mtb}})^{-5/3}$ and L_γ is the photon's luminosity. Adopting the slim-disk model for the super-Eddington MAD, we estimate $L_\gamma = 2\pi \int_{r_s}^{r_t} r Q_{\text{rad}} dr \approx 1.1 \times 10^{46} (M_{\text{bh}}/10^{7.7} M_\odot) \log(r_t/r_s) \text{ erg s}^{-1}$, where $Q_{\text{rad}} \approx 3.7 \times 10^{17} \text{ erg/cm}^2 (M_{\text{bh}}/10^{7.7} M_\odot)^{-1} (r/r_s)^{-2}$ is the radiative cooling rate (Watarai 2006). We then estimate $\xi_{\text{bl}} \sim 0.21 (\eta_{\text{cr}}/0.1) (M_{\text{bh}}/10^{7.7} M_\odot)^{-3/2} (m_*/M_\odot)^2 (r_*/R_\odot)^{-3/2} \log^{-1}(r_t/r_s)$. Adopting $L_\gamma = \eta_{\text{MAD}} \dot{M} c^2$ similarly, we estimate $\xi_{\text{bl}} \sim$

$0.67 (\eta_{\text{cr}}/0.1)(\eta_{\text{MAD}}/0.15)^{-1}$. In the super-Eddington MAD state, the baryon loading is less than unity and therefore different from the jetted TDE case where ξ_{bl} ranges from 1 to 100 (Baerwald et al. 2015; Senno et al. 2017; Biehl et al. 2018). In the RIAFs, the baryonic loading parameter is estimated to be $\xi_{\text{bl}} = L_p/L_{\text{RIAF}} \sim 1.0 (\eta_{\text{cr}}/0.1)(\dot{m}/0.01)(\alpha/0.1)^{-2}$, where we adopt $L_p = \eta_{\text{cr}}\dot{M}c^2$ and $L_{\text{RIAF}} \approx 0.1(\dot{m}/\alpha^2)\dot{M}c^2$ (Mahadevan 1997). In this case, ξ_{bl} is of the order of unity or less in the RIAFs of both the non-MAD and MAD cases.

The neutrino energy generation rate inferred from the observed isotropic neutrino flux is estimated to be $\rho_\nu \sim 10^{43-44} \text{ erg Mpc}^{-3} \text{ yr}^{-1}$ for the 10 – 100 TeV range as seen in Figure 1 of Murase & Fukugita (2019). In our present model, the neutrino energy generation rate of the RIAF phase is estimated to be $\rho_\nu = L_{\nu,\text{bol}}t_{\text{RIAF}}\mathcal{R}_V \sim 2.1 \times 10^{43} \text{ erg Mpc}^{-3} \text{ yr}^{-1} (\eta_\nu/0.1)(\xi_{\text{bl}}/1.0)(L_{\text{RIAF}}/1.3 \times 10^{42} \text{ erg s}^{-1})(M_{\text{bh}}/10^7 M_\odot)^{-3/5}(t_{\text{RIAF}}/1.7 \times 10^9 \text{ s})(\mathcal{R}_V/10^{-7} \text{ Mpc}^{-3} \text{ yr}^{-1})$, where we adopt $\dot{m} = 0.01$ for $\dot{M} = \dot{m}\dot{M}_{\text{Edd}}$, $L_{\nu,\text{bol}} = \eta_\nu L_p = \eta_\nu \xi_{\text{bl}} L_{\text{RIAF}}$ is the bolometric luminosity of the neutrinos, $\eta_\nu \sim 0.1$ is the proton to neutrino conversion efficiency, and \mathcal{R}_V is the volumetric TDE rate (cf. Dai & Fang 2017). In the case of super-Eddington MAD, the energy generation rate is $\rho_\nu = L_{\nu,\text{bol}}t_{\text{Edd}}\mathcal{R}_V \sim 2.3 \times 10^{43} \text{ erg Mpc}^{-3} \text{ yr}^{-1} (\eta_{\text{cr}}/0.1)(\xi_{\text{bl}}/0.67)(L_p/6.3 \times 10^{45} \text{ erg s}^{-1})(M_{\text{bh}}/10^{7.7} M_\odot)^{-3/2}(t_{\text{mtb}}/2.5 \times 10^7 \text{ s})(\mathcal{R}_V/10^{-9} \text{ Mpc}^{-3} \text{ yr}^{-1})$, where we adopt $L_{\nu,\text{bol}} = \eta_\nu L_p = \eta_\nu \xi_{\text{bl}} L_{\text{Edd}}$ and we assume that $\sim 1\%$ of the observed TDE rate experiences the super-Eddington MAD state. The RIAFs of both the non-MAD and MAD states and the super-Eddington MAD state can potentially contribute to the diffuse neutrino flux.

It is interesting to refer to the redshift evolution of TDE rates. According to Kochanek (2016), the TDE rate rapidly decreases with redshift, mainly because the black hole mass density decreases with redshift. The TDEs that occurred at $z = 0$ are the main source contributing to the diffuse neutrino flux. However, there is some ambiguity as to how the frequency of TDEs evolves with redshift because most of the identified TDEs occur at a

lower redshift than unity. We will discuss in detail how much the TDE remnants contribute to the diffuse neutrino flux in a forthcoming paper.

In the standard TDE theory, the RIAF phase would start at $t_{\text{RIAF}} \sim 10^9$ s after the stellar disruption (see equation 15 for details). However, if a star approaches an SMBH on a marginally hyperbolic orbit, a small fraction of debris mass should have negative binding energy and therefore falls back to the SMBH at a much smaller rate than the Eddington rate (Hayasaki et al. 2018). In this case, the RIAF phase starts at about two orders of magnitude earlier than the standard case, that is, $\sim 10^7$ s. This can enhance the energy generation rate, even if the event rate of marginally hyperbolic TDEs would be subdominant.

The heavier nuclei exist for a main-sequence star with mass greater than $1 M_{\odot}$ as well as for a WD case. Tidal disruption of such a massive star can show a significant enhancement of the nitrogen-to-carbon ratio due to the CNO cycle (Kochanek 2016; Gallegos-Garcia et al. 2018). These carbon/nitrogen anomalies should, therefore, be observational evidence for TDEs caused by the massive stars. The increase of the nucleon number density is responsible for the larger energy density of the plasma, resulting in higher energy of accelerated protons. This excess energy possibly helps one to diagnose whether a disrupted star originates from the massive stars on the main sequence.

When a star is tidally disrupted, about a half of the stellar debris is unbound and ejected from the system. It collides with an ambient matter, forming a shock to produce nonthermal radiations like supernova remnants (Guillochon et al. 2016). Such electromagnetic afterglows are potentially observed after the neutrino emission is detected because the peak time of the afterglows is 10^{3-4} yr depending on parameters such as the ambient density.

Let us discuss how one can observationally identify the neutrino emissions from the

TDEs based on our models. The neutrino horizon is defined as $D_\nu = \sqrt{L_\nu/(4\pi\mathcal{S})}$, because $L_\nu/4\pi d^2$, where d is the distance between the earth and the source, should be greater than or equal to the sensitivity \mathcal{S} for the neutrino detection. The IceCube sensitivity of neutrinos below 100 TeV is roughly given by $5 \times 10^{-11} \text{ erg s}^{-1} \text{ cm}^2$ for an observation of a few months (IceCube Collaboration, et al. 2019). We can evaluate the horizon of 0.1 – 100 TeV neutrinos as $D_\nu \approx 1 \text{ Gpc} (L_\nu/L_{\text{Edd}})^{1/2} (\mathcal{S}/[5 \times 10^{-11} \text{ erg s}^{-1} \text{ cm}^2])^{-1/2}$ in the case of $M_{\text{bh}} = 10^{7.7} M_\odot$. We then estimate the detection rate of the MAD state as $\sim 3.4 \times 10^{-1} \text{ yr}^{-1} (n_{\text{gal}}/0.003 \text{ Mpc}^{-3}) (D_\nu/220 \text{ Mpc})^3 (\mathcal{R}/10^{-5} \text{ yr}^{-1})$, where we adopt $L_\nu = E_{\nu,\text{pk}} L_{E_{\nu,\text{pk}}} \sim 3.0 \times 10^{44} \text{ erg s}^{-1} (\eta_{\text{cr}}/0.1)$ (see panel (b) of Figure 2) and $\mathcal{R} = 10^{-5} \text{ yr}^{-1}$ as the TDE rate per galaxy. In the case of RIAF phase, we can similarly evaluate the horizon as $D_\nu \approx 460 \text{ Mpc} (L_\nu/L_{\text{Edd}})^{1/2} (\mathcal{S}/[5 \times 10^{-11} \text{ erg s}^{-1} \text{ cm}^2])^{-1/2}$ in the case of $M_{\text{bh}} = 10^7 M_\odot$. The detection rate is then estimated to be $\sim 1.2 \times 10^{-3} \text{ yr}^{-1} (n_{\text{gal}}/0.003 \text{ Mpc}^{-3}) (D_\nu/34 \text{ Mpc})^3 (\mathcal{R}/10^{-5} \text{ yr}^{-1})$, where we adopt $L_\nu = E_{\nu,\text{pk}} L_{E_{\nu,\text{pk}}} \sim 7.0 \times 10^{42} \text{ erg s}^{-1} (\eta_{\text{cr}}/0.1)$ (see panel (a) of Figure 2).

A star approaches an SMBH on a Keplerian orbit, and it is tidally disrupted around the pericenter, where the gravitational wave (GW) can be also emitted with a burst-like variation (Kobayashi et al. 2004). The GW frequency is then given by $f = 2\sqrt{GM_{\text{bh}}/r_{\text{p}}^3} \sim 1.3 \times 10^{-3} \text{ Hz} (\beta/1)^{3/2} (m_*/M_\odot)^{1/2} (r_*/R_\odot)^{-3/2}$. We evaluate the GW horizon D_{gw} of the TDE case using the quadruple formula as $D_{\text{gw}} = (1/2)(m_*/M_{\text{bh}})(r_{\text{S}}/r_{\text{p}})(r_{\text{S}}/h) \sim 9.4 \text{ Mpc} (\beta/1)(h/10^{-21})^{-1} (M_{\text{bh}}/10^7 M_\odot)^{2/3} (m_*/M_\odot)^{4/3} (r_*/R_\odot)^{-1}$, where h is the GW amplitude. *LISA*, *DECIGO*, and *BBO* can detect the amplitude $h \gtrsim 10^{-21}$ for the frequency range $10^{-4} \text{ Hz} \lesssim f \lesssim 0.1 \text{ Hz}$, $h \gtrsim 10^{-22}$ for the frequency range $f \gtrsim 10^{-2} \text{ Hz}$, and $h \gtrsim 10^{-22}$ for the frequency range $f \gtrsim 10^{-3} \text{ Hz}$, respectively (Moore, Cole & Berry 2015). The detection rate is conservatively estimated to be $\sim 2.5 \times 10^{-5} \text{ yr}^{-1} (n_{\text{gal}}/0.003 \text{ Mpc}^{-3}) (D_{\text{gw}}/9.4 \text{ Mpc})^3 (\mathcal{R}/10^{-5} \text{ yr}^{-1})$ for the *LISA* range. If we adopt $\beta = 4$ for a solar-type star, then $f \gtrsim 10^{-3} \text{ Hz}$ and thus $D_{\text{gw}} \sim$

$380 \text{ Mpc} (M_{\text{bh}}/10^7 M_{\odot})^{2/3}$ with $h = 10^{-22}$. The detection rate is conservatively $0.1 \text{ yr}^{-1} (n_{\text{gal}}/0.003 \text{ Mpc}^{-3}) (\mathcal{R}_{\beta}/10^{-6} \text{ yr}^{-1})$ for the *DECIGO* and *BBO* range, where we simply define $\mathcal{R}_{\beta} = \mathcal{R}/\beta^2$ because the cross section between the SMBH and the star is proportional to $1/\beta^2$. Stone et al. (2013) derived the GW amplitude as having a steeper β dependence, and suggested the tidal disruption of a WD by an IMBH is a more promising GW source candidate for the advanced LIGO bands, although the event rate of WD-IMBH disruptions still includes a large ambiguity. From the viewpoints of the multi-messenger observations, there should be a time lag between the GW and neutrino detections because of the different emission site and mechanism. The GWs arise from the strong compression of the star at the tidal disruption, while the neutrinos can emit in the super-Eddington MAD state, radiatively inefficient MAD state, and the RIAF phase after the debris circularization phase. Therefore, the GW signals and associated X-ray flares (Kobayashi et al. 2004; Guillochon et al. 2009) could be precursors of neutrino and corresponding photon emissions in the two states and the RIAF phase.

5. Conclusions

We have investigated the high-energy emissions from the stellar debris moving around SMBHs in TDEs. There are four main evolutionally phases after the tidal disruption of a star: the debris circularization phase, the super-Eddington accretion phases of both the MAD and non-MAD states, the sub-Eddington accretion phase, and the RIAF phases of both the MAD and non-MAD states, respectively (see equation 16). We have found that there are three promising sites, where the high-energy particles can be produced from the TDR: the super-Eddington accretion phase of the MAD state and the RIAF phases of both the non-MAD and MAD states. Our main conclusions are summarized as follows:

1. High-energy particles at the first (strongest) shock during the debris circularization

phase are unlikely to be produced, because the mass fallback rate exceeding the Eddington rate makes both the Compton drag and the proton-proton collision cooling very efficient. Since the shocked region is far from the black hole, the magnetic field is relatively weak. The weak magnetic field is another reason why the stochastic acceleration of the protons becomes inefficient.

2. High-energy particles during the super-Eddington accretion phase of the non-MAD state are unlikely to be produced because of very efficient proton-proton collision cooling and Compton drag, even though the stochastic acceleration of the protons is more efficient because of the much stronger magnetic field than that of the first shock case.
3. Neutrinos and gamma-ray photons are produced by pions not only in the super-Eddington MAD scenario but also in the RIAF scenarios of both the non-MAD and MAD cases. However, the gamma-ray photons cannot escape from the source because of the large optical depth in the super-Eddington MAD state and of the very efficient pair production in the RIAF cases.
4. In the RIAF phase, the protons can be accelerated up to $\sim 0.45 \text{ PeV} (M_{\text{bh}}/10^7 M_{\odot})^{5/3}$ with the other given appropriate parameters. The neutrino energy emitted at the peak of the spectrum is then estimated as $\sim 0.35 \text{ PeV} (M_{\text{bh}}/10^7 M_{\odot})^{5/3}$. The neutrino emission is proportional to $t^{-10/3}$, which is steeper than the standard TDE decay rate. This indicates that one can potentially identify whether a RIAF that existed around an SMBH has a TDE origin or not.
5. In the super-Eddington MAD state, the stronger magnetic field than in the non-MAD case makes it possible to accelerate the protons up to ultrarelativistic energies. The dominant process to prevent the protons from accelerating strongly depends on the black hole mass. If the black hole mass is larger than $\sim 10^{7.7} M_{\odot}$, the synchrotron

cooling is the most dominant process. In this case, the protons are accelerated up to an energy of $\sim 0.35 \text{ PeV} (M_{\text{bh}}/10^{7.7} M_{\odot})^{41/48}$ with the other given appropriate parameters. The neutrino energy at the peak of the spectrum is then estimated as $\sim 67 \text{ TeV} (M_{\text{bh}}/10^7 M_{\odot})^{41/48}$. Otherwise, the Compton drag is the more efficient process. In this case, the resultant energy of the protons increases at most up to $\sim 2.2 \text{ TeV} (M_{\text{bh}}/10^{7.4} M_{\odot})^{89/12}$.

6. In the super-Eddington MAD state, if $M_{\text{bh}} \gtrsim 10^{7.7} M_{\odot}$, the neutrino light curve is proportional to $t^{-65/24}$, which is steeper than the standard TDE $t^{-5/3}$ decay rate. On the other hand, it follows the $t^{-5/3}$ decay rate with energy more than 1 TeV if $10^{7.4} M_{\odot} \lesssim M_{\text{bh}} < 10^{7.7} M_{\odot}$. In both cases, the neutrino luminosity is of the order of the Eddington limit or the luminosity exceeding it. Such a high neutrino luminosity and characteristic light curve give us the ability to judge whether the TDE disk is in the MAD state or not.
7. In the radiatively inefficient MAD state, the stronger magnetic field than in the non-MAD case makes it possible to accelerate the protons up to $25 \text{ PeV} (M_{\text{bh}}/10^7 M_{\odot})^{-1/12}$. The neutrino energy estimated at the peak of the spectrum is then $4.8 \text{ PeV} (M_{\text{bh}}/10^7 M_{\odot})^{-1/12}$. The resultant neutrino luminosity is, however, too weak to be detected with the current sensitivity of IceCube.

Acknowledgments

The authors thank the anonymous referee for fruitful comments and suggestions. The authors also thank Abraham Loeb and Kohta Murase for their helpful comments and suggestions. This research has been supported by Basic Science Research Program through the National Research Foundation of Korea (NRF) funded by the Ministry of Education

(NRF-2017R1D1A1B03028580 to K.H.) and also by JSPS KAKENHI (Grant No.18H01232 to R.Y.).

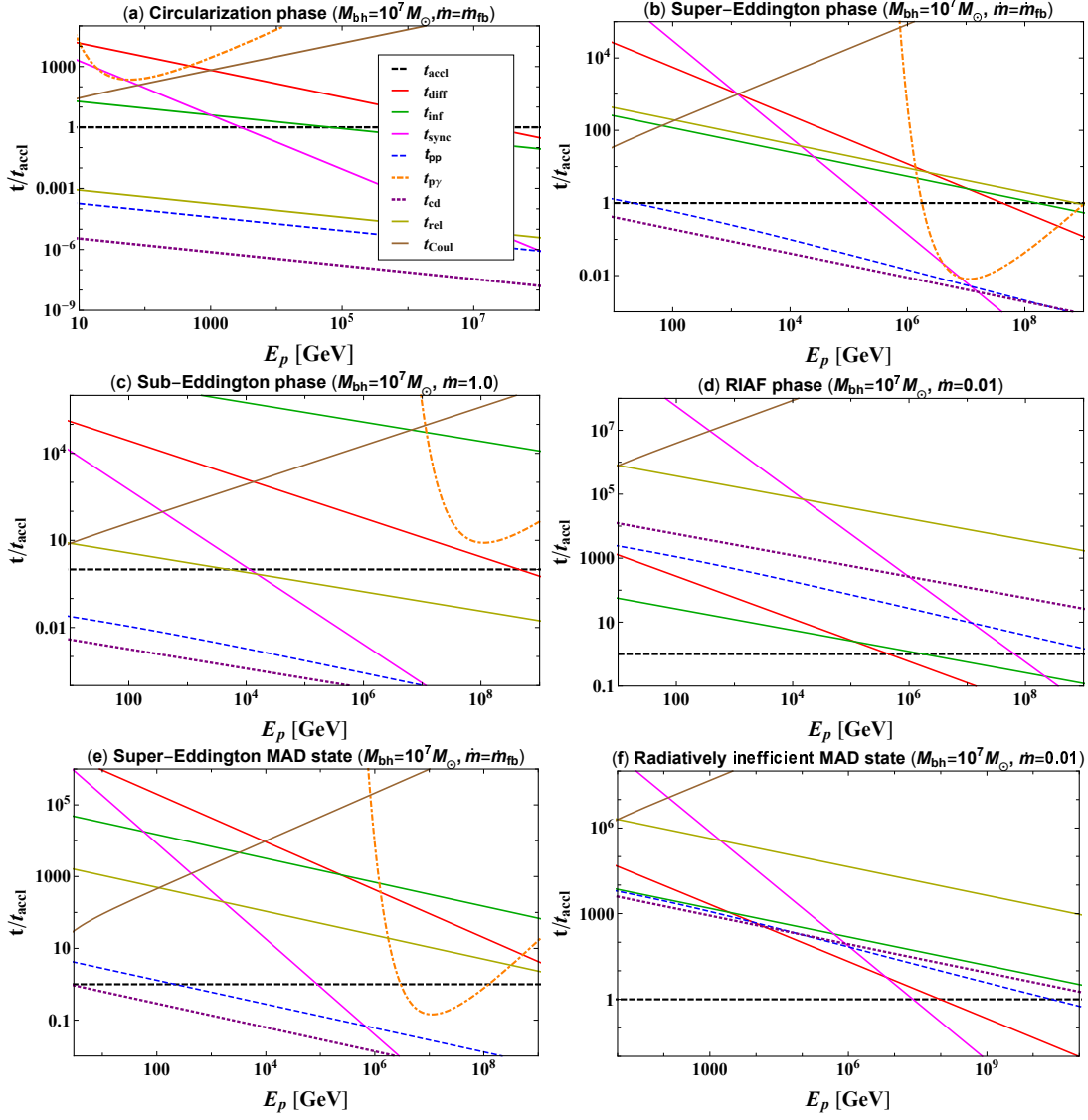


Fig. 1.— Dependence of the characteristic timescales normalized by the acceleration time on the proton energy for the six sites in the TDR. In each panel, the dashed black line denotes the time of stochastic acceleration of relativistic protons (t_{acc}). The solid red, solid dotted, dotted magenta, dashed blue, dashed-dotted orange, solid purple, solid yellow, and solid brown lines are the diffusion time (t_{diff}), infall time (t_{inf}), synchrotron cooling time (t_{sync}), proton-proton collision cooling (t_{pp}), photo-meson cooling time ($t_{p\gamma}$), Compton drag time (t_{Cd}), relaxation time (t_{rel}), and Coulomb collision time (t_{Coul}), respectively. Panels (a)-(f) show the cases of the first shock during debris circularization, super- and sub-Eddington accretion phases, RIAF phase, super-Eddington MAD state, and radiatively inefficient MAD state, respectively.

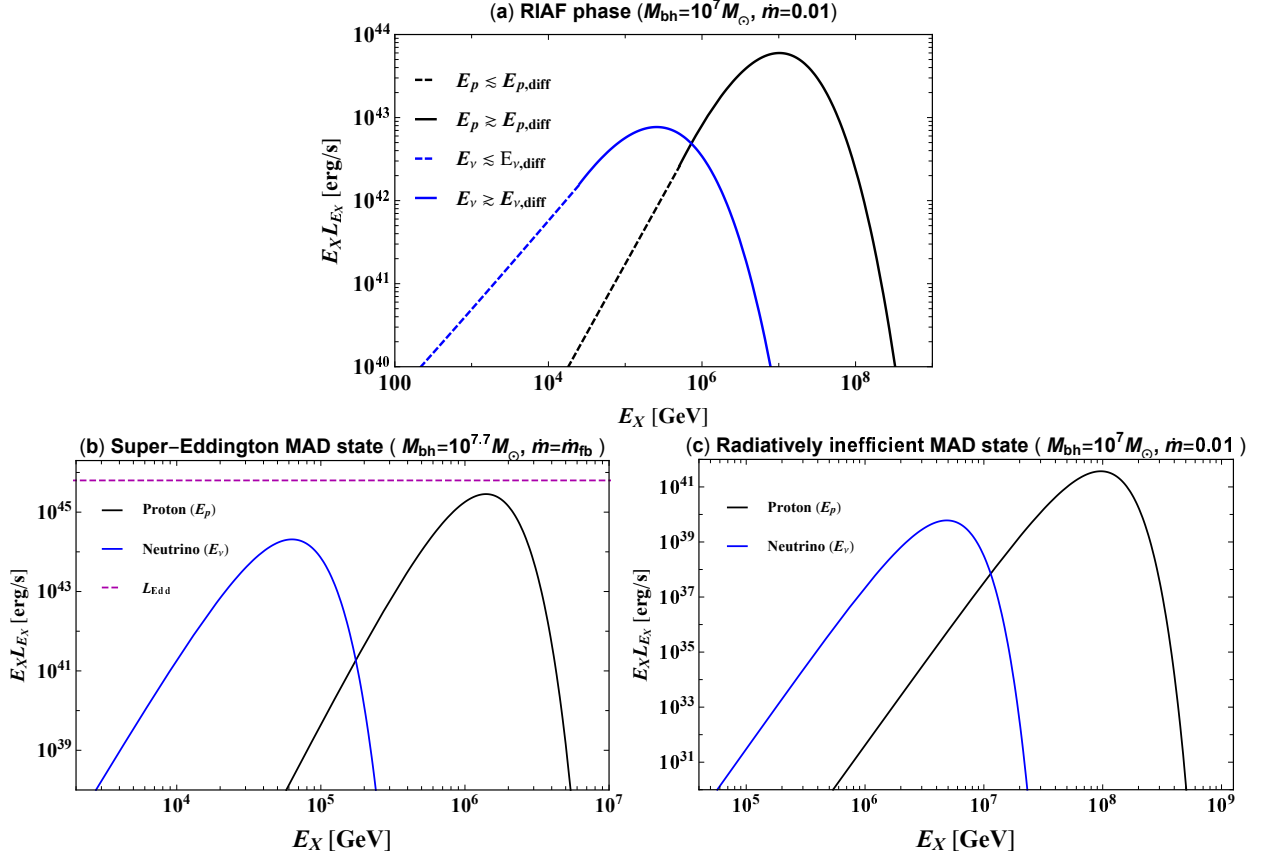


Fig. 2.— The differential luminosity spectra of the protons and neutrinos emitted from the RIAF phase (non-MAD state), super-Eddington MAD state, and radiatively inefficient MAD state. In all the three panels, the black and blue lines show the differential luminosity spectra of the proton and neutrino, respectively. Here \dot{m} , E_p , and E_ν are the normalized mass fallback rate, proton energy, and neutrino energy, respectively, and $\eta_{\text{cr}} = 0.1$ is adopted as the injection efficiency. In panel (a), the dotted (solid) black and blue lines show the differential luminosity spectra of lower (higher) energy than $E_{p,\text{diff}}$ (see equation 47) and $E_{\nu,\text{diff}} = 0.05E_{p,\text{diff}}$, respectively. Panel (b) depicts the differential luminosity spectra of super-Eddington MAD state, where the dashed line denotes the Eddington luminosity $L_{\text{Edd}} \simeq 6.3 \times 10^{45} \text{ erg/s} (M_{\text{bh}}/10^{7.7} M_\odot)$. Panel (c) shows the case of the radiatively inefficient MAD state.

REFERENCES

- Aab, A., Abreu, P., Aglietta, M., et al. 2017, *Journal of Cosmology and Astro-Particle Physics*, 2017, 38
- Aartsen, M. G., Abbasi, R., Abdou, Y., et al. 2013, *Physical Review Letters*, 111, 021103
- Abramowicz, M. A., Czerny, B., Lasota, J. P., & Szuszkiewicz, E. 1988, *ApJ*, 332, 646
- Alves Batista, R., & Silk, J. 2017, *Phys. Rev. D*, 96, 103003
- Alexander, K. D., Berger, E., Guillochon, J., Zauderer, B. A., & Williams, P. K. G. 2016, *ApJ*, 819, L25
- Arcavi, I., Gal-Yam, A., Sullivan, M., et al. 2014, *ApJ*, 793, 38
- Auchettl, K., Guillochon, J., & Ramirez-Ruiz, E. 2017, *ApJ*, 838, 149
- Baerwald, P., Bustamante, M., & Winter, W. 2015, *Astroparticle Physics*, 62, 66
- Becker, P. A., Le, T., & Dermer, C. D. 2006, *ApJ*, 647, 539
- Biehl, D., Boncioli, D., Lunardini, C., & Winter, W. 2018, *Scientific Reports*, 8, 10828
- Biehl, D., Boncioli, D., Fedynitch, A., et al. 2018, *A&A*, 611, A101
- Bisnovatyi-Kogan G. S., Ruzmaikin A. A., 1974, *Ap&SS*, 28, 45
- Bonnerot, C. et al, 2016, *MNRAS*, 455, 2253
- Bonnerot, C., Rossi, E. M., & Lodato, G. 2017, *MNRAS*, 464, 2816
- Brown, G. C., Levan, A. J., Stanway, E. R., et al. 2015, *MNRAS*, 452, 4297
- Burrows, D. N., Kennea, J. A., Ghisellini, G., et al. 2011, *Nature*, 476, 421

- Cenko, S. B., Krimm, H. A., Horesh, A., et al. 2012, *ApJ*, 753, 77
- Chornock, R., Berger, E., Gezari, S., et al. 2014, *ApJ*, 780, 44
- Dai, L., McKinney, J. C., & Miller, M. C. 2015, *ApJ*, 812, L39
- Dai, L., & Fang, K. 2017, *MNRAS*, 469, 1354
- Dai, L., McKinney, J. C., Roth, N., et al. 2018, *ApJ*, 859, L20.
- Dermer, C. D., Miller, J. A., & Li, H. 1996, *ApJ*, 456, 106
- Donley J. L., Brandt W. N., Eracleous M., Boller T., 2002, *AJ*, 124, 1308
- Evans, C. R., & Kochanek, C. S. 1989, *ApJ*, 346, L13
- Farrar, G. R., & Gruzinov, A. 2009, *ApJ*, 693, 329
- Farrar, G. R., & Piran, T. 2014, arXiv:1411.0704
- Gallegos-Garcia, M., Law-Smith, J., & Ramirez-Ruiz, E. 2018, *ApJ*, 857, 109
- Gezari, S., Martin, D. C., Milliard, B., et al. 2006, *ApJ*, 653, L25
- Gezari, S., Chornock, R., Rest, A., et al. 2012, *Nature*, 485, 217
- Guépin, C., Kotera, K., Barausse, E., et al. 2018, *A&A*, 616, A179.
- Guillochon, J., Ramirez-Ruiz, E., Rosswog, S., & Kasen, D. 2009, *ApJ*, 705, 844
- Guillochon, J., McCourt, M., Chen, X., Johnson, M. D., & Berger, E. 2016, *ApJ*, 822, 48
- Hayasaki, K., Stone, N., Loeb, A. 2013, *MNRAS*, 434, 909
- Hayasaki, K., Stone, N., Loeb, A. 2016, *MNRAS*, 461, 3760
- Hayasaki, K., Zhong, S., Li, S., et al. 2018, *ApJ*, 855, 129.

- Holoien, T. W.-S., Prieto, J. L., Bersier, D., et al. 2014, MNRAS, 445, 3263
- Holoien, T. W.-S., Kochanek, C. S., Prieto, J. L., et al. 2016, MNRAS, 455, 2918
- Hung, T., Gezari, S., Blagorodnova, N., et al. 2017, ApJ, 842, 29
- IceCube Collaboration, et al., 2019, arXiv e-prints, arXiv:1902.05792
- Jiang, Y.-F., Guillochon, J., & Loeb, A. 2016, ApJ, 830, 125
- Jiang Y.-F., Stone J., Davis S. W., 2017, arXiv e-prints, arXiv:1709.02845
- Kelner, S. R., Aharonian, F. A., & Bugayov, V. V. 2006, Phys. Rev. D, 74, 034018
- Kimura, S. S., Murase, K., & Toma, K. 2015, ApJ, 806, 159
- Kobayashi, S., Laguna, P., Phinney, E. S., & Mészáros, P. 2004, ApJ, 615, 855
- Kochanek, C. S. 2016, MNRAS, 458, 127
- Kochanek, C. S. 2016, MNRAS, 461, 371
- Komossa S., Bade N., 1999, A&A, 343, 775
- Lodato, G., King, A. R., & Pringle, J. E. 2009, MNRAS, 392, 332
- Lunardini, C., & Winter, W. 2017, Phys. Rev. D, 95, 123001
- Mahadevan, R. 1997, ApJ, 477, 585
- Maksym, W. P., Ulmer, M. P., Eracleous, M. C., Guennou, L., & Ho, L. C. 2013, MNRAS, 435, 1904
- Marshall M. D., Avara M. J., McKinney J. C., 2018, MNRAS, 478, 1837
- McKinney J. C., Tchekhovskoy A., Blandford R. D., 2012, MNRAS, 423, 3083

- McKinney J. C., Dai L., Avara M. J., 2015, MNRAS, 454, L6
- Mészáros, P. 2017, Annual Review of Nuclear and Particle Science, 67, 45
- Merritt, D., Alexander, T., Mikkola, S., & Will, C. M. 2010, Phys. Rev. D, 81, 062002
- Moore C. J., Cole R. H., Berry C. P. L., 2015, CQGra, 32, 15014
- Murase, K. 2008, American Institute of Physics Conference Series, 201
- Murase, K., & Fukugita, M. 2019, Phys. Rev. D, 99, 63012.
- Murase, K., Guetta, D., & Ahlers, M. 2016, Physical Review Letters, 116, 071101
- Murase, K., & Ioka, K. 2013, Physical Review Letters, 111, 121102
- Narayan R., Igumenshchev I. V., Abramowicz M. A., 2003, PASJ, 55, L69
- Narayan, R., & Yi, I. 1994, ApJ, 428, L13
- Narayan, R., & Yi, I. 1995, ApJ, 452, 710
- Phinney, E. S. 1989, in IAU Symp. 136, The Center of the Galaxy, ed. M. Morris (Dordrecht: Kluwer Academic Publishers), 543
- Pfeffer, D. N., Kovetz, E. D., & Kamionkowski, M. 2017, MNRAS, 466, 2922
- Piran, T., Svirski, G., Krolik, J., Cheng, R. M., & Shiokawa, H. 2015, ApJ, 806, 164
- Rees, M. J., 1998, Nature 333, 523
- Saxton, R. D., Read, A. M., Esquej, P., et al. 2012, A&A, 541, A106
- Senno, N., Murase, K., & Mészáros, P. 2017, ApJ, 838, 3.
- Shiokawa, H., Krolik, J. H., Cheng, R. M., Piran, T., & Noble, S. C. 2015, ApJ, 804, 85

- Stone, N., Sari, R., Loeb, A., 2013, MNRAS, 435, 1809
- Stone, N., Metzger, B. D. 2016, MNRAS, 455, 859
- Stawarz, L., & Petrosian, V. 2008, ApJ, 681, 1725
- Thompson, C., & Blaes, O. 1998, Phys. Rev. D, 57, 3219
- van Velzen, S., Farrar, G. R., 2014, ApJ, 792, 53
- van Velzen, S., Anderson, G. E., Stone, N. C., et al. 2016, Science, 351, 62
- Vinkó, J., Yuan, F., Quimby, R. M., et al. 2015, ApJ, 798, 12
- Wang, J., Merritt, D., 2004, ApJ, 600, 149
- Wang, X.-Y., Liu, R.-Y., Dai, Z.-G., & Cheng, K. S. 2011, Phys. Rev. D, 84, 081301
- Wang, X.-Y., & Liu, R.-Y. 2016, Phys. Rev. D, 93, 083005
- Wang, J.-M., & Zhou, Y.-Y. 1999, ApJ, 516, 420
- Watarai K.-ya ., 2006, ApJ, 648, 523
- Waxman, E. 1995, Phys. Rev. Lett., 75, 386.
- Waxman, E., & Loeb, A. 2001, Physical Review Letters, 87, 071101
- Zauderer, B. A., Berger, E., Soderberg, A. M., et al. 2011, Nature, 476, 425
- Zhang, B. T., Murase, K., Oikonomou, F., & Li, Z. 2017, Phys. Rev. D, 96, 063007